

Modelling of Passive Mode Locking in Semiconductor Quantum Dot Lasers

Adam Pywowarczuk

A Thesis
in
The Department
of
Electrical and Computer Engineering

Presented in Partial Fulfillment of the Requirements
for the Degree of Master of Applied Science (Electrical and Computer Engineering) at
Concordia University
Montreal, Quebec, Canada

November 2022

© Adam Pywowarczuk, 2022

CONCORDIA UNIVERSITY
School of Graduate Studies

This is to certify that the thesis prepared

By: Adam Pywowarczuk

Entitled: Modelling of Passive Mode Locking in Semiconductor Quantum Dot Lasers

and submitted in partial fulfillment of the requirements for the degree of

Master of Applied Science (Electrical and Computer Engineering)

complies with the regulations of the University and meets the accepted standards with respect to originality and quality.

Signed by the final Examining Committee:

_____	Chair
<i>Dr. Sébastien Le Beux</i>	
_____	Examiner
<i>Dr. Pablo Bianucci</i>	
_____	Examiner
<i>Dr. Sébastien Le Beux</i>	
_____	Supervisor
<i>Dr. John Xiupu Zhang</i>	

Approved by _____
Dr. Yousef Shayan, Chair
Department of Electrical and Computer Engineering

_____ 2022 _____
Dr. Mourad Debbabi, Dean
Gina Cody School of Engineering and Computer Science

ABSTRACT

Modelling of Passive Mode Locking in Semiconductor Quantum Dot Lasers

Adam Pywowarczuk

Quantum Dots (QDs) have been the subject of much attention due to their highly discrete band structure which allows for the emission of highly monochromatic light. Lasers can be made to produce pulses using a technique called mode-locking (ML), but QDs lasers which have not intentionally been mode-locked have still been observed exhibiting the same pulsing behaviour. The purpose of this research is to create a simulation of the dynamics of a QD laser to attempt to better understand the mechanism behind the observed mode-locking effect.

To study this, a simulation of a QD laser system was created in COMSOL Multiphysics 5.4 based on a theoretical model which uses a quantum perturbation theory to provide a detailed treatment of carrier-light interactions to model the impact that four wave-mixing (FWM) has on the electric field. This simulation was used to recreate results from simulations based on a time domain travelling wave (TDTW) model as well as experimental data to assess how well the perturbation theory model is able to match the data.

It was found that the simulation was able to produce results indicating the presence of lasing, but due to only simulating a single dot it is unable to properly show inhomogeneous gain broadening and mode-locking. Though this model shows potential for a variety of applications, it will need to be further enhanced to include multiple QDs and cavity modes to act as a more accurate and effective tool.

Acknowledgements

I would like to thank Dr. John X. Zhang for his supervision during this project, and both Xiaoran Xie and Gaowen Chen for their help and feedback at various points during my work.

I also wish to thank Fr. Robert Pierre Louis for all the spiritual guidance he has provided during the years spent on this project.

Most importantly, I would like to thank my parents, Karen and Victor.

Table of Contents

List of Figures.....	vi
List of Tables.....	ix
List of Acronyms.....	x
Chapter 1 – Introduction to Quantum Dot Lasers.....	1
1.1 Introduction.....	1
1.2 Motivations and Contributions.....	5
1.3 Organization of Thesis.....	7
Chapter 2 – Theoretical Model.....	9
2.1 Introduction.....	9
2.2 Properties of Quantum Dots.....	9
2.3 Laser Theory.....	13
2.4 TDTW Model.....	18
2.5 Perturbation Theory Model.....	24
Chapter 3 – Simulation Details.....	32
3.1 Introduction.....	32
3.2 Geometry.....	32
3.3 Functions.....	34
3.4 Differential Equations.....	38
3.5 Parameters.....	41
3.6 Post-Processing.....	42
Chapter 4 – Examination of the Proposed Perturbation Theory Model.....	45
4.1 Introduction.....	45
4.2 RF Spectra.....	45
4.3 Time-Domain Pulses.....	50
4.4 Optical Spectrum.....	52
Chapter 5 – Investigation.....	55
5.1 Introduction.....	55
5.2 RF Spectra.....	55
5.3 Time Domain Pulses.....	57
5.4 Optical Spectrum.....	61
Chapter 6 – Conclusion.....	64
References.....	67
Appendix.....	72

List of Figures

Figure 1.1 Diagrams of the DOS functions for a bulk semiconductor (a), a quantum well (b), a quantum wire (c), and a quantum dot (d) [1]

Figure 1.2 Diagram comparing the time-domain intensity of a) a non-ML laser and b) a non-ML laser

Figure 1.3 Demonstration of the gain-loss cycle seen in a two-section ML laser [9]

Figure 2.1 Representation of relaxation during SK growth. The material with large lattice constant a_1 is in the material with small lattice constant a_0 . This creates non-uniform spacing between the clusters [28]

Figure 2.2 Diagram illustrating the impact of varying dot sizes on inhomogeneous gain broadening [9]

Figure 2.3 Diagram of a two-level laser

Figure 2.4 Diagram of a three-level laser

Figure 2.5 Diagram of a four-level laser

Figure 2.6 Diagram of the energy level diagram used in this model, including all relevant transitions and their lifetimes

Figure 2.7 Diagram showing how the electronic density of states is modelled using a Gaussian function based on the inhomogeneous broadening effect, illustrating the broadening as Δ_{inh} increases

Figure 3.1 Image of the QD geometry, as shown within the simulation

Figure 3.2 Image of the entities included in the model's geometry

Figure 3.3 The piece-wise function used to model the effects of spectral hole burning

Figure 3.4 Image of the functions used to calculate the important variables in this model

Figure 3.5 The function for the chemical potential for electrons, illustrating how globally inaccessible variables are included as arguments

Figure 3.6 Diagram of the domain on which all three domain ODEs are calculated

Figure 3.7 Image of the constraints set up to maintain conservation in the carrier rate equations

Figure 3.8 Demonstration of the use of the sum() function to add up the saturation of each mode

Figure 3.9 The time dependent step set up to solve the domain ordinary differential equations

Figure 4.1 RF beat note spectra for a 250 μm long InAs/InGaAs QD laser, from published TDTW simulation results [14]

Figure 4.2 RF beat note spectra for a 1 mm long InAs/InGaAs QD laser, from published experimental results [14]

Figure 4.3 RF beat note spectra for a 250 μm long InAs/InGaAs QD laser, from perturbation theory simulation

Figure 4.4 RF beat note spectra for a 1 mm long InAs/InGaAs QD laser, from perturbation theory simulation

Figure 4.5 Time domain electric field behaviour in a InAs QD laser using an injection current of a) 803 mA, b) 827 mA, c) 832 mA, d) 840 mA, e) 872 mA, and f) 910 mA, from published results [19]

Figure 4.6 Time domain electric field behaviour in a InAs QD laser using an injection current of a) 803 mA, b) 827 mA, c) 832 mA, d) 840 mA, e) 872 mA, and f) 910 mA, from perturbation theory simulation

Figure 4.7 Optical power spectra for a passively mode-locked InAs/GaAs QD laser using injection current densities ranging from 70-350 A/cm², from published results [20]

Figure 4.8 Optical power spectra for a passively mode-locked InAs/GaAs QD laser using injection current densities ranging from 70-350 A/cm², from perturbation theory simulation

Figure 5.1 Small segments of the time domain electric field behaviour of a 3.5 mm InAs QD laser with an injection current of a) 803 mA, b) 827 mA, c) 832 mA, d) 840 mA, e) 872 mA, and e) 910 mA

Figure 5.2 Simulated carrier dynamics of a 3.5 mm InAs QD with an injection current of 803 mA

Figure 5.3 Time domain electric field behaviour of a InAs/GaAs QD with an injection current density of 70 A/cm² as modelled using the perturbation theory simulation

List of Tables

Table 3.1 Physical dimensions used to define the geometry of the QDs

Table 3.2 Carrier energies and transition energy values for InGaAs/GaAs QDs [26]

Table 3.3 Carrier energies and transition energy values for InAs/InP QDs [27]

Table 3.4 List of all important constants used within the model

Table 3.5 List of all parameters which are used in all versions of the model

Table 4.1 List of specific parameters used to simulate results published by Bardella *et al.* [14]

Table 4.2 List of specific parameters used to simulate results published by Tierno *et al.* [19]

Table 4.3 List of specific parameters used to simulate results published by Majid *et al.* [20]

List of Acronyms

CBE	Chemical Beam Epitaxy
DOS	Density Of States
ES	Excited State
FWM	Four Wave Mixing
GS	Ground State
GVD	Group Velocity Dispersion
ML	Mode-Locking
MLL	Mode-Locked Laser
MBE	Molecular Beam Epitaxy
QD	Quantum Dot
QW	Quantum Well
OFC	Optical Frequency Comb
PECVD	Plasma-Enhanced Chemical Vapour Deposition
SA	Saturable Absorber
SCH	Separate Confinement Heterostructure
SHB	Spatial/Spectral Hole Burning
SK	Stranski-Krastanov
SPM	Self-Phase Modulation
TDTW	Time Domain Travelling Wave
WL	Wetting Layer

Chapter 1 – Introduction to Quantum Dot Lasers

1.1 Introduction

Lasers are a very highly valued technology due to their ability to act as highly monochromatic and coherent light sources. Lasers primarily operate through stimulated emission, so the amplified light will be monochromatic due to one specific transition stimulating further emissions at the same wavelength. However, this is an idealization, and in reality we see a broader range of wavelengths depending on different factors. The desire for greater monochromaticity motivates the creation of lasers which use quantum dots (henceforth QDs), due to their unique density of states (henceforth DOS). The DOS of a material is a function which represents the distribution of allowed states which carriers can occupy at different energy values, and it depends on a variety of different factors. A technique called quantum confinement, wherein a dimension of the material is reduced until carriers within the material experience quantum effects, can be used to manipulate the DOS of the material. Quantum dots, which create a highly discrete DOS through quantum confinement applied in three dimensions, are one such example of this approach. Other structures such as quantum wells (confined in 1 dimension) and quantum wires (confined in 2 dimensions) also take advantage of these effects to modify their DOS, but QDs offer the most discrete DOS function. As shown in Figure 1.1, [1] QDs have Dirac delta-like DOS function, which limits the number possible transitions within a certain energy range and thus limits the range of emitted wavelengths. Real implementations of QDs do not match up with this idealized picture, due to effects such as inhomogeneous broadening and the fact that the band gap of the QDs can vary with dot size [2], but they consistently perform better than bulk semiconductors in terms of gain, threshold current, jitter, and filamentation [3][4][5].

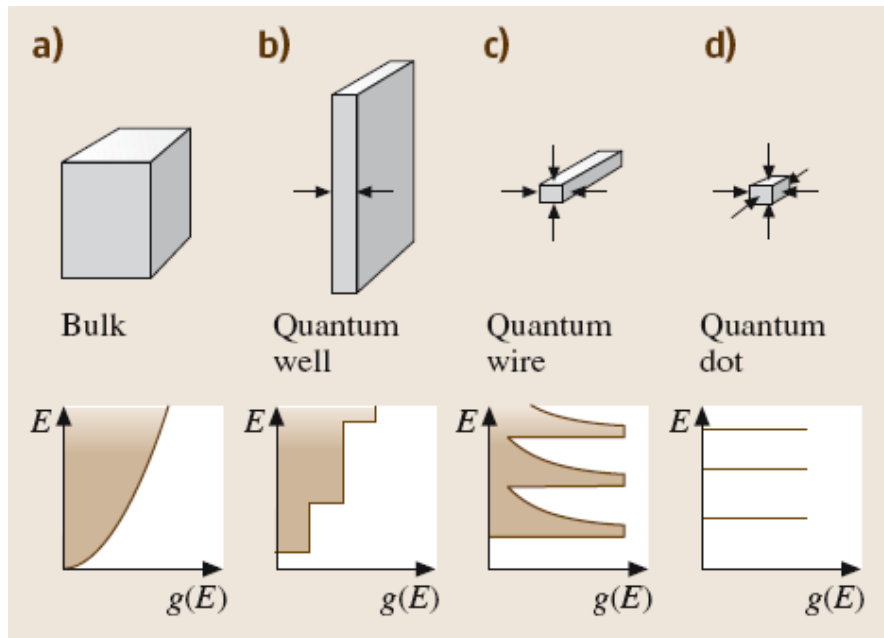


Figure 1.1 Diagrams of the DOS functions for a bulk semiconductor (a), a quantum well (b), a quantum wire (c), and a quantum dot (d) [1]

Lasers using QDs as the active medium have been proposed as early 1976 by Dingle *et al.* [6], with multiple researchers successfully producing QD lasers in the 90s [6][7]. Of particular interest are QD lasers operating at 1.3 μm , which is the wavelength commonly used for communications. For this reason we are also looking for lasers which can emit periodic pulses, which are helpful due to higher bit rate transmission, optical clock recovery, ultrafast signal processing, and the generation of optical frequency combs (OFC). There are multiple different methods used for creating pulsing lasers, and the one commonly focused on is mode-locking (ML). Mode-locking refers to a technique where multiple modes of the standing wave within the laser cavity are locked together by controlling their phases to cohere. Due to the matching of their phases the waves will interfere destructively in much of the cavity, save for a region of highly constructive interference. This region of constructive interference will travel back and forth through the cavity periodically, creating pulses that repeat on a fixed duration. A depiction of this behaviour and how it differs from standard lasing behaviour is shown in Figure 1.2.

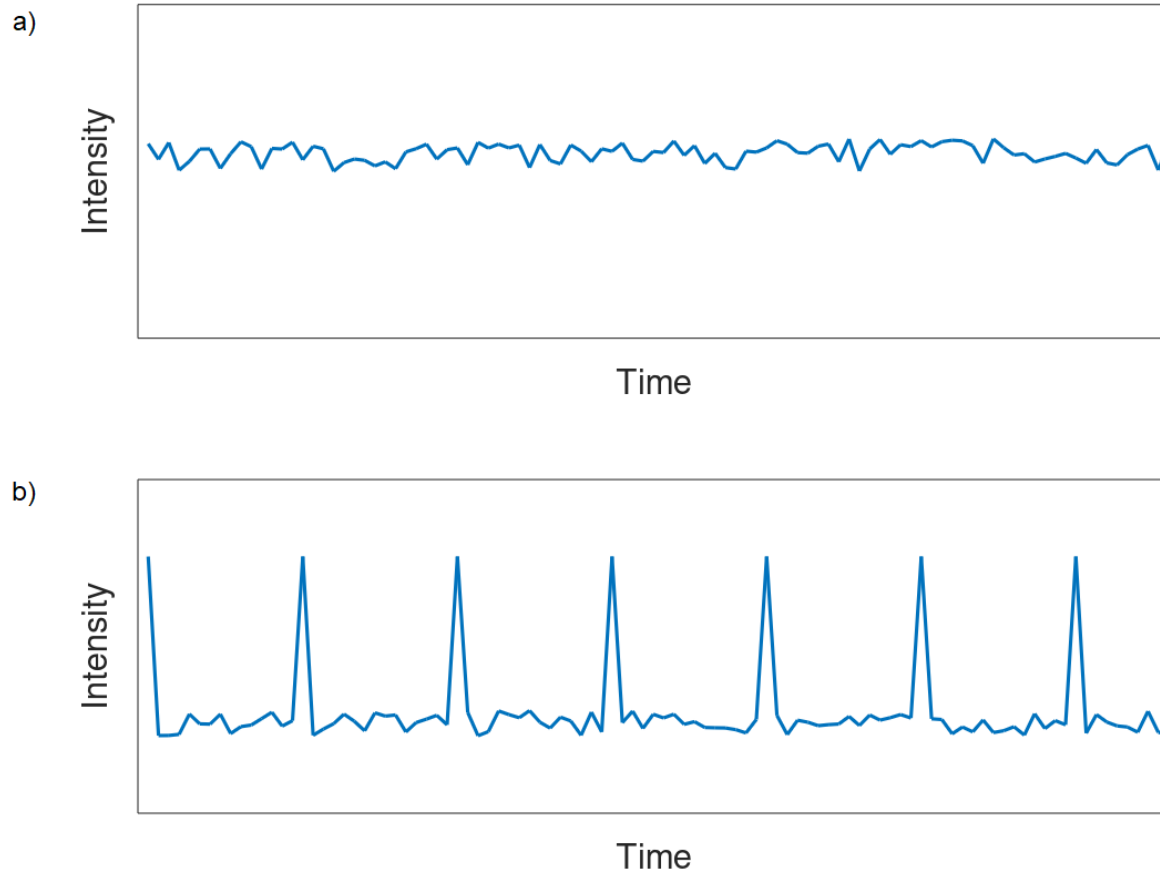


Figure 1.2 Diagram comparing the time-domain intensity of a) a non-ML laser and b) a non-ML laser

Mode-locking can be performed actively (using an electric signal or other external effects) or passively (through the properties of the device itself). The most common method for passive ML involves creating a laser cavity with two sections: the active lasing medium, and a saturable absorber (SA), which is a material that absorbs less light as its intensity increases. In general the loss of the cavity will be greater than the gain, but due to the SA the leading edge of the pulse will saturate the absorber more quickly than the peaks, causing a brief period of high gain. This creates a cycle where the loss periodically exceeds the gain, at which point the pulse envelope becomes inverted [8]. This cycle is illustrated in Figure 1.3.

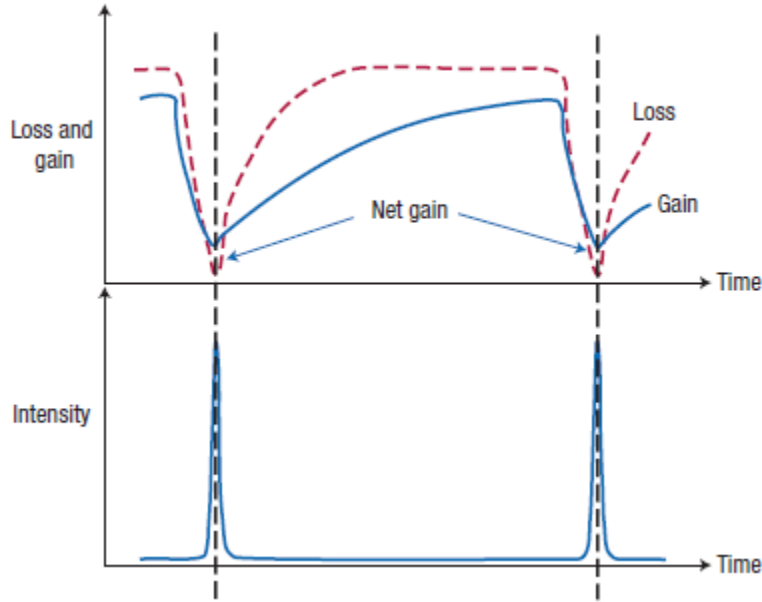


Figure 1.3 Demonstration of the gain-loss cycle seen in a two-section ML laser [9]

However, committing to a laser with two sections limits our design options, so single-section ML lasers are preferred. The theoretical basis for mode-locking in single section lasers is not clearly understood, though it has been experimentally realized in multiple configurations, demonstrating high output power [10] and high temperature stability [11][12]. The purpose of this project is to investigate the causes of this observed mode-locking by developing a theoretical model and testing it through computer simulations to see how well it matches with these experimental results, as well as other theoretical predictions.

Popular candidates for the main cause of this effect are spatial hole burning (SHB), the Kerr-lens effect, self-phase modulation (SPM), group velocity dispersion (GVD), and four-wave mixing (FWM) [13]. This research primarily focuses on the contributions of FWM, which refers to a nonlinear response of the medium prompted by the optical field within the cavity. Four-wave mixing specifically refers to three optical fields of frequencies ω_1 , ω_2 , and ω_3 being superimposed to create a wave at a fourth frequency ω_4 . As such, the frequency of this fourth wave must satisfy the relationship $\omega_4 = \omega_1 \pm \omega_2 \pm \omega_3$. For example, in one specific case we can have two photons that generate two new photons, which corresponds to the specific relationship $\omega_1 + \omega_2 = \omega_3 + \omega_4$. However, this process must still adhere to conservation of momentum by ensuring that $p_{1,2} = p_{3,4}$. If we further define a frequency difference Ω and specify that $\omega_1 = \omega_2$, $\omega_3 = \omega_1 + \Omega$, and $\omega_4 = \omega_1 -$

Ω we will find that $p_{1,2} = \frac{(\omega_1 + \omega_2)}{c} = \frac{2\omega_1}{c}$ and $p_{3,4} = \frac{(\omega_3 + \omega_4)}{c} = \frac{(\omega_1 + \Omega) + (\omega_1 - \Omega)}{c} = \frac{2\omega_1}{c}$. This will ensure that the momentum before and after the mixing will be the same, meaning that momentum will be conserved. These conditions are also chosen so that the phases of the waves are properly locked in order to generate pulses.

This effect is of particular interest as most existing theoretical models, particularly those explored by Bardella *et al.* [14][15][16] use a time domain travelling wave (TDTW) approach. Though these models have shown good results, they do not include a detailed treatment of FWM, and also have difficulties including other minor effects such as GVD and SPM. For this research, a modified TDTW wave model similar to the one proposed Chow *et al.* [17][18] is used in combination with carrier rate equations derived by Jiao *et al.* [13]. What differentiates this from other TDTW models is that the equations modelling the electric field is derived from a detailed quantum mechanical picture of electron-light interaction, leading to a more detailed treatment of the effects of FWM than previous simulations. The results of this approach, as modelled using COMSOL Multiphysics 5.4, have been compared with both results from simulations of the previous model [14] and reported experimental data from single section mode-locked QD lasers [19][20] to demonstrate how a model which properly incorporates the effects of FWM can produce the same mode-locking that has been seen in previous research both theoretically and experimentally.

If the role that FWM plays in the observed mode-locking phenomenon is better understood, then it can aid further research into and development of pulsed QD lasers. A robust simulation of a QD laser can also be used to make predictions and evaluate which properties can produce desirable results, helping to design future devices.

1.2 Motivations and Contributions

This project was primarily motivated by acquiring a better understanding of the mechanism behind mode-locking in single section QD lasers. Multiple approaches to ML using either external signals or specialized two section cavities are well understood, but reported examples of ML in single section lasers are not well understood. Most common theoretical studies of this phenomenon use approaches which neglect the importance of many effects.

Multiple previous publications have explored the role which effects such as both spatial and spectral hole burning (SHB) [21], the Kerr lens effect [3], or non-linearities within the cavity [22] play in mode-locking, but there has not been as much inquiry into the role of FWM. This research's emphasis on the influence of FWM can help fill in the blanks of our understanding of the observed mode-locking mechanism. The goal of this research is to properly evaluate the impact of these effects, and to see if they are a significant contributor to the thus far unexplained ML.

Previous models, in particular one put forth by Bardella *et al.* in multiple publications [14][15][16], have achieved good results in simulating such devices by using a simple TDTW approach. This model will henceforth be referred to as the TDTW model. This approach, however, does not significantly emphasize contributions from FWM and various other possible key factors. Due to these deficiencies, other possible approaches need to be investigated to make continued progress. To build on this foundation, further theoretical models which have been previously published by Jiao *et al.* [13] and Chow *et al.* [17][18] were also considered and have been elaborated on and expanding to build a complete model with a more thorough treatment of FWM than previous simulations. Contributions from these papers, such as the rate equations and gain switching, are used alongside other modifications which are added to avoid drawbacks or inconvenient assumptions such as thermal equilibrium. The final model is able to incorporate the effects of FWM through the application of quantum perturbation theory, and thus this model will be referred to as the perturbation theory model.

The resulting simulation can then be used to attempt to reproduce published results, both experimental [19][20] and from other simulations [14]. These results can be used to evaluate the accuracy of the theoretical model and assess the significance of FWM in passive mode-locking, as well as to propose ideas for future research and device designs.

This thesis primarily focuses on the simulation of this theoretical model. The major contributions are:

- 1) Simulation of the carrier dynamics, electrical field behaviour, and optical spectrum of quantum dots.

- 2) Comparison of a new perturbation theory-based theoretical model emphasizing the contributions of FWM to the ML mechanism in these devices to previous proposed models, both in terms of their backgrounds and the produced results.
- 3) Comparison of published experimental data to the results of both the perturbation theory simulation and TDTW models using the appropriate parameters to assess the accuracy of the models and the importance of FWM.
- 4) Suggestions for future improvements to the simulation and possible areas of inquiry based on results from the simulation.

1.3 Organization of Thesis

This introductory chapter provides a basic explanation of QD lasers, mode-locking, some of the current challenges in the field, and some of the possible applications of such research. The reasoning for using QDs as the active medium of a laser over bulk materials is explained, as well as the applications and why the use of mode-locking to generate pulses is desirable. From there, the current limitations in ML are discussed, including methods of both active and passive mode locking. In particular, passive mode-locking within single section lasers, as well as current issues with our theoretical understanding of this phenomenon are discussed. A new theoretical model and simulation based on quantum perturbation theory is proposed as a solution.

Chapter 2 goes into detail on the theoretical background of this topic. The TDTW model used by Bardella *et al.*, included both its strengths and flaws, is examined and from this a new model to explore other causes of mode locking is developed. This model is a modified version of the previous, using a similar approach but with a more detailed treatment of electron-light interactions using quantum perturbation theory, which better reflects the contributions of four-wave mixing.

Chapter 3 discusses the implementation of the perturbation theory model in COMSOL Multiphysics 5.4. A basic outline of the equations and how they have been implemented, as well as a detailed description of each segment of the simulation will be presented. The simulation will also be converted into MATLAB code, which will be reproduced in full in the Appendix. A

second MATLAB program which was used to process the data and produce figures will also be explained.

Chapter 4 presents the published results which were compared with the perturbation theory simulation. Three different published results were used as a basis of comparison: first, data sets from the TDTW [14]; then, experimental data from an InAs-based QD laser operating at wide range of injection currents [19]; and finally, experimental data from an InP-based QD laser [20].

Chapter 5 presents the results from the perturbation theory simulation, and contrasts them with the published results discussed in Chapter 4. Both the perturbation theory simulation discussed in Chapter 3 and the TDTW model discussed in Chapter 2 were used to replicate this published data as closely as possible by using the appropriate values and parameters. The output from the improved simulation is analyzed in detail, in terms of how it compares with both the TDTW simulation and the real experimental results, as well as the implications of the results.

Chapter 6 acts as a summary of the previous chapters and all major findings from this work. Based on the findings from perturbation theory simulation, an assessment of the simulation's capabilities and weaknesses is made, and plans for ways to improve it as well as future research into single-section ML QD lasers is proposed.

Chapter 2 – Theoretical Model

2.1 Introduction

To start with some of the basic theory relating to quantum dots and their properties are discussed, as well as some of the basic theory behind lasing, will be explained. From here, the reason why quantum dots are desirable for laser applications will be made clear.

Section 2.2 gives a detailed explanation of the basic properties and current theoretical understanding of QDs, as well as some of the optoelectric devices which can be made with QDs. From there, section 2.3 will go into detail on laser theory, and explain different ways that the carrier dynamics in these systems can be modelled with rate equations. The next sections look at more detailed models for QD lasers specifically. In particular, section 2.4 will look over some of the previous published TDTW-centred models of ML behaviour in single-section QD lasers and analyze them. Section 2.5 will then go on propose a model based on quantum perturbation theory, and explain the important implications. Finally, the conclusion in section 2.6 will summarize the important results.

2.2 Properties of Quantum Dots

QDs are a specific application of a technique referred to as quantum confinement. This is a method used to take advantage of quantum effects, as bulk materials and other objects at large scales are governed by classical mechanics while quantum mechanics only plays a role at very small scales. Quantum confinement is simply a reduction of the spatial dimensions of the material which leads to a reduction of the carriers' degrees of freedom and thus a reduction of the allowed phase space [23]. This technique is often used with indirect band gap semiconductors, where the conduction and valence bands are separated in both energy and phase space. The control over the allowed phase space provided by quantum confinement makes it possible to create a direct band gap where it is easier for transitions to occur, which is one example of the types of band gap engineering made possible through this technique. As these quantum effects, such as the uncertainty principle, can have a significant effect on the optoelectronic properties of the material, varying the size and shape of the structure allows control of important properties such as emission wavelength and carrier lifetimes [24].

A quantum dot refers specifically to a structure where quantum confinement has been performed in all three spatial dimensions, as opposed to simply one (quantum wells) or two (quantum wires, or quantum dashes). There are a variety of different methods for producing these structures, and the way they are produced can have a significant impact on their properties. Common methods include co-sputtering, plasma-enhanced chemical vapour deposition (PECVD), Chemical Beam Epitaxy (CBE), and Molecular Beam Epitaxy (MBE) [23]. Techniques involving the implantation of ions onto a substrate make it very easy to control the growth of the layers, but it is also important to be mindful of the substrate which is used. As the dots, or nanostructures, grow within pores in the substrate, the material used for the substrate and the structure of its pores can have a significant impact on the size and distribution of the dots [25]. The size of the dots in particular is very important for band gap engineering, as the spacing between the energy levels within the dots get smaller as the dots themselves get bigger [26][27].

Growth of QDs through epitaxy has been studied in detail, and is typically classified in terms of three different “modes”. These modes depend on interface energies and the lattice constant of the materials used. The most commonly used mode of QD growth for laser applications is the Stranski-Krastanov (SK) mode, in which one semiconductor with a large lattice constant is deposited onto one with a much smaller lattice constant. Due to the mismatch in the lattice sizes, a large amount of strain is created, and to release this strain the deposited atoms “relax” into clusters [28], these clusters becoming the QDs. A diagram explaining this relaxation mechanism is shown in Figure 2.1.

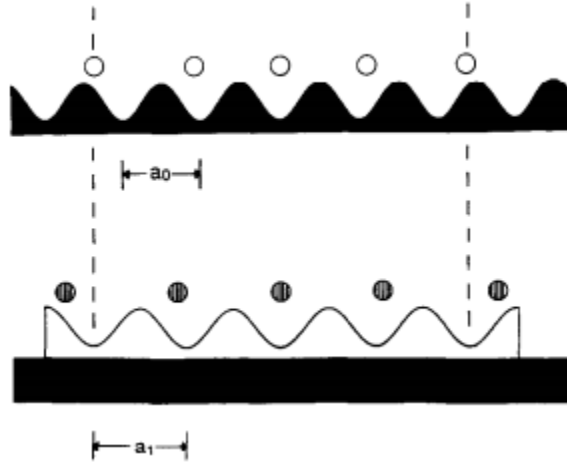


Figure 2.1 Representation of relaxation during SK growth. The material with large lattice constant a_1 is grown in the material with small lattice constant a_0 . This creates non-uniform spacing between the clusters [28]

The main reason QDs are ideal as a lasing medium is that the reduction of phase space in all three dimensions due to quantum confinement gives them a more discrete band structure than other materials. Because of the limited phase space, there are only a limited number of transitions which can occur, which is useful for stimulated emission (see section 2.3). However, this is an idealization, and there are multiple other effects that need to be taken into consideration in reality.

The most prominent of these effects that need to be considered when modelling QDs is inhomogeneous broadening. As mentioned earlier, the energy of the emissions from the QDs depends on their size. Due to the limitations of all known techniques for growing QDs, it is very difficult to control any variation in their sizes, and since QDs with different sizes allow different transitions, a system with a broad distribution of QD sizes will also have a broad range of possible emissions, limiting monochromaticity.

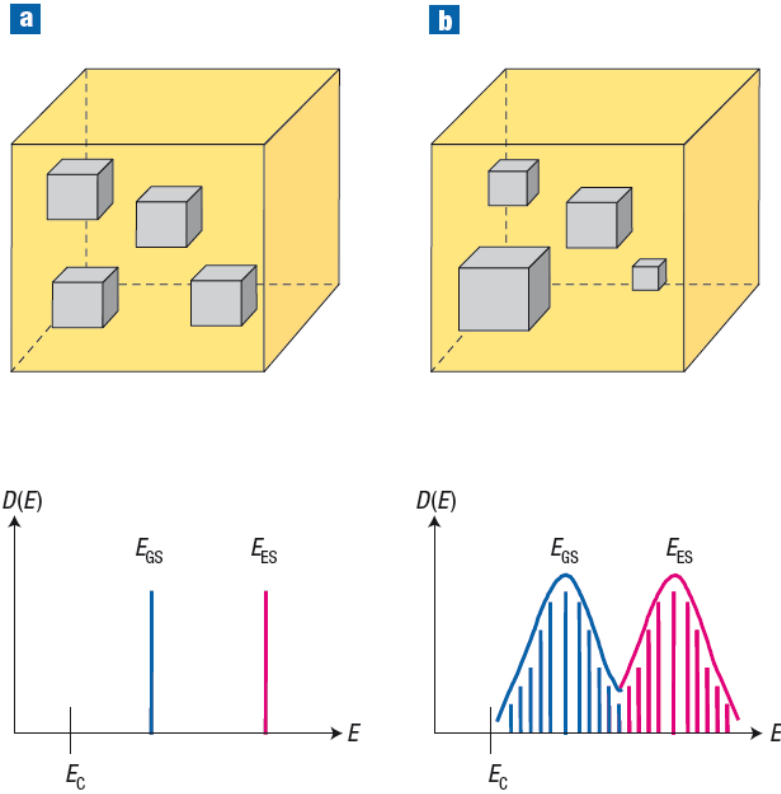


Figure 2.2 Diagram illustrating the impact of varying dot sizes on inhomogeneous gain broadening [9]

Due to this broadening effect, large increases in bandwidth have been observed. For example, QD semiconductor optical amplifiers designed with bandwidths of 2-dB and 10-dB were observed exhibit broadening effects as large as 150 nm and 300 nm [29].

Another important factor is the photon bottleneck effect. Due to the limitations in the phase space of the QDs, there is a corresponding drop in the electron-photon scattering rate [30]. The scattering rates affects the relaxation times in the QD states, making excited carries take longer to relax than in bulk material. This different carrier behaviour will need to be taken into consideration when studying the carrier dynamics in a QD laser. For example, carriers in QDs have been observed to have a fast recovery on the order of 1 ps, followed by a slow decay on the order of 100 ps [31]. Ultrafast recovery on the order of 100 fs has also been observed, and is commonly attributed to Auger scattering [32][33]. If these fast carrier dynamics can be taken

advantage of, lasers with very high repetition rates can be designed, so Auger scattering should be included in any model to be sure this effect is taken into account.

2.3 Laser Theory

LASER is an acronym which stands for Light Amplification by Stimulated Emission of Radiation. It is a device which allows for the production of high intensity, highly monochromatic light by taking advantage of a phenomenon referred to as stimulated emission. This describes the tendency for electrons in an excited state to interact with photons carrying the same amount of energy, causing the electrons to lose their energy by emitting a photon. Because of the nature of this interaction, the new outgoing photon will have the same wavelength and the original in-going one. The emitted photon can then go on to stimulate further similar emissions, as can the next emitted photon and the photon after it. These simulated emissions will eventually create a very large number of photons of the exact same wavelength, amplifying the intensity of the original photon many times over via the principle of superposition.

To create a laser, first the system must achieve what is called a population inversion. In a general distribution of carriers, we would expect the lower energy, unexcited states to be more highly populated than the higher energy, excited states. A population inversion is the opposite, or “inversion” of this default configuration; the higher energy states are much more populated than the lower energy levels. In the context of band theory, this would mean a large number of electrons in the conduction band and a large number of holes in the valence band. Such a configuration is difficult to achieve, and is very difficult to maintain for continuous operation, as the electrons and holes will want to recombine as quickly as they can. This is commonly achieved through forward biasing of a pn-junction.

When speaking about lasing, the state which the excited electrons occupy is often referred to as the excited state (ES), and the lower energy state that they decay down to is referred to as the ground state (GS). However, looking at only these two states is a very oversimplified picture which does not work out in reality.

If we were to attempt to model a laser with only these two levels (two level laser), we would start by defining the number of carriers in the GS as N_0 and the number of carriers in the ES as N_1 .

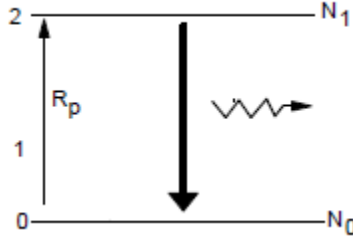


Figure 2.3 Diagram of a two-level laser

From here, we can work on creating rate equations for this system. Here, R_p represents the number of carriers excited by the pump per second, and γ_{10} represents the decay rate from level 1 to level 0. This will be measured in 1/s, and is the inverse of the lifetime for N_1 and the recombination time for N_0 .

$$\frac{dN_1}{dt} = R_p(N_0 - N_1) - \gamma_{10}N_1 \quad (2.1)$$

$$\frac{dN_0}{dt} = \gamma_{10}N_1 - R_p(N_0 - N_1) \quad (2.2)$$

This is a very simple system of equations for the two levels, which conveniently also leaves us with $\frac{dN_1}{dt} = -\frac{dN_0}{dt}$, ensuring that the number of carriers is conserved. Any carriers that are removed from N_0 must be added to N_1 through the pump, and any that are added to N_0 are removed from N_1 through radiative decay. However, as convenient as this model is, it is severely limited as a population inversion cannot be properly realized.

Before starting the pump, out of the total number of carriers in the system N_{tot} , all of them will be in the ground state N_0 and none of them will be in the excited state N_1 . Thus the initial conditions for our system of equations will be $N_1(0) = 0$ and $N_0(0) = N_{tot}$, and from these it follows that $\frac{dN_1}{dt} = R_p N_{tot}$ at $t = 0$. Since we've defined N_{tot} to be the total number of the carriers

of the system, we can also say that $N_{\text{tot}}(t) = N_0(t) + N_1(t)$, and that this value will be constant for all time values. We can also find the steady state solution for N_1 by setting the derivatives to 0.

This leaves us with $N_1 = \frac{R_p N_0}{R_p + \gamma_{10}}$, which can be further rearranged into $\frac{N_1}{N_0} = \frac{1}{1 + \frac{\gamma_{10}}{R_p}}$. This fraction

$\frac{N_1}{N_0}$ tells us how much larger the number of carriers in the excited state is than those in the ground state. As such, if we want our steady state behaviour to be a population inversion, we want to

have $\frac{N_1}{N_0} > 1$, but looking at the expression we derived we will always have a value less than 1,

even for very small γ_{10} and very large R_p . This tells us that the steady state behaviour of this system will always leave us with slightly more carriers in the ground state, meaning that this model is insufficient for showing a system where population inversion, and thus lasing, is maintained for a long period of time.

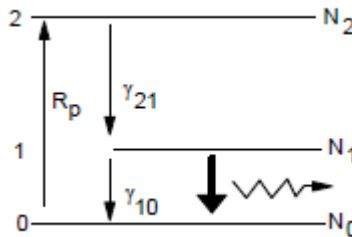


Figure 2.4 Diagram of a three-level laser

In that case, we can try to add more energy levels to improve this model. Instead of having all of the excited carriers decay straight down to the ground state, we will instead add an intermediate state in the middle. The excited carriers will rapidly decay down to this intermediate state without emitting a photon, and then finally undergo a much slower radiative transition down to the ground state.

We can now create a new set of rate equations for such a system, using very similar reasoning to our previous model:

$$\frac{dN_2}{dt} = R_p(N_0 - N_2) - \gamma_{21}N_2 \quad (2.3)$$

$$\frac{dN_1}{dt} = \gamma_{21}N_2 - \gamma_{10}N_1 \quad (2.4)$$

$$\frac{dN_0}{dt} = \gamma_{10}N_1 - R_p(N_0 - N_2) \quad (2.5)$$

Once again, we can define $N_{\text{tot}} = N_0 + N_1 + N_2$, and we can use the same initial conditions and the same method for finding steady state solutions. As we're finding the steady state solutions, we can also introduce some assumptions to simplify some of the work. As mentioned in the description of this system, the transition from level 2 down to level 1 is very fast, so the transition rate γ_{21} is a very large value, typically much larger than what we would expect for the pumping rate R_p . Similarly, due to the fast decay, the population in level 2 will always be much lower than the population of the ground state. Assuming $\gamma_{21} \gg R_p$ and $N_0 \gg N_2$, after we set the derivative to 0, we can simplify 2.3 into $0 = R_p N_0 - \gamma_{21} N_2$, which leaves us with $N_2 = \frac{R_p}{\gamma_{21}} N_0$.

Next we can find the steady state solution of the intermediate level. Setting the derivative to 0 leaves us with $N_1 = \frac{\gamma_{21}}{\gamma_{10}} N_2$, which we can then combine with the other steady state solution to create an expression for the population inversion. Since carriers decay out of level 3 very quickly, and these decays are nonradiative, we should be focusing on level 1 instead. Knowing that $\frac{N_1}{N_0} = \frac{R_p}{\gamma_{10}}$, we can see that the population inversion depends on both the pumping rate and the radiative decay rate. It is indeed possible to maintain a population inversion with this model, but it requires a high pump rate and a low decay rate, which makes such a system very inefficient.

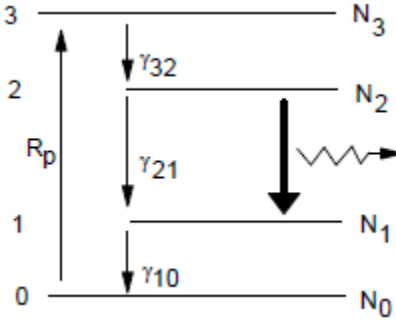


Figure 2.5 Diagram of a four-level laser

Since we still want better results, we can try again by adding another energy level. This is very similar to the three-level model, but this time there is another intermediate energy level that the carrier will move into after its radiative transition. From this last intermediate level, it then quickly decays back down to the ground state non-radiatively. We can now create a system of four rate equations for this model:

$$\frac{dN_3}{dt} = R_p(N_0 - N_3) - \gamma_{32} N_3 \quad (2.6)$$

$$\frac{dN_2}{dt} = \gamma_{32} N_3 - \gamma_{21} N_2 \quad (2.7)$$

$$\frac{dN_1}{dt} = \gamma_{21} N_2 - \gamma_{10} N_1 \quad (2.8)$$

$$\frac{dN_0}{dt} = \gamma_{10} N_1 - R_p(N_0 - N_3) \quad (2.9)$$

Now, we can check the steady state behaviour of this model and see if maintaining a population inversion is possible. By setting all of the time derivatives to 0, we end up with $N_2 = \frac{\gamma_{32}}{\gamma_{21}} N_3$ and $N_1 = \frac{\gamma_{21}}{\gamma_{10}} N_2$. Since the radiative transition we are focusing on in this model is from level 2 to 1, we are looking only at the population inversion between 2 and 1. Using these steady state solutions, we find $\frac{N_2}{N_1} = \frac{\gamma_{10}}{\gamma_{21}}$.

Just like in the three-level model, our radiative decay is very slow, so its decay rate is very small, whereas the decay rate from 1 to 0 is very large, which means that this model will

leave us with a population inversion that will be much greater than 1 at all times with no dependence on the pump rate, like with the previous model. This system of equations finally leaves us with solutions that will maintain a population inversion for a long period of time. As such, four-level or five-level models are commonly used in detailed treatments of lasing.

2.4 TDTW Model

Bardella *et al.* have written extensively about modelling mode-locking in QD lasers, in particular using a TDTW approach [14][15][16]. This approach models the electric field in the cavity as a travelling wave in the time domain, starting from some of Maxwell's equations.

$$\nabla \times E = -j\omega\mu_0 H \quad (2.10)$$

$$\nabla \times H = j\omega(\epsilon_0\epsilon_r E + P) + J = j\omega\epsilon_0\epsilon_r E + j\omega P + J \quad (2.11)$$

By combining the differential forms of the Maxwell-Faraday equation and Ampere's circuital law, with terms added for the polarization and the stochastic current density, we can create a second order differential equation.

$$\frac{1}{-j\omega\mu_0} \nabla^2 E = j\omega\epsilon_0\epsilon_r E + j\omega P + J \quad (2.13)$$

We can start to simplify this equation a bit to help us narrow down the solution. First, we will not be able to strictly define any transverse electric (TE) or transverse magnetic (TM) modes, so the laser cavity will only have quasi-TE and quasi-TM modes, both pointing in the same direction. We will define this direction as z , and since our electric field is only varying in that one direction we can replace the del operator with a simple derivative with respect to z . The polarization term which we've added can also be expressed in terms of the electrical field and the electronic susceptibility, via $P = \epsilon_0\chi E$, which further helps us to simplify this equation.

$$\frac{\partial^2 E(z, \omega)}{\partial z^2} = \frac{-\omega^2 n^2}{c^2} E(z, \omega) - \omega^2 \mu_0 \chi E(z, \omega) + j\omega \mu_0 J \quad (2.14)$$

For the sake of simplicity, we can also define $\beta(\omega) = \frac{\omega n}{c}$ (where $\beta(\omega_0) = \beta_0$). We can then find a solution for this equation, and use a Fourier transform to convert it from the spatial domain into the frequency domain.

$$E(z, \omega_0 + \Omega) = \sqrt{\frac{\omega_0 \mu_0}{\beta_0}} \left(E^f(z, \Omega) e^{-j\beta_0 z} + E^b(z, \Omega) e^{j\beta_0 z} \right) \quad (2.15)$$

For the model, a forward (f) and backward (b) propagating wave solution is used. In the transformed version of the solution, Ω is the relative frequency, which is defined as $\Omega = \omega - \omega_0$ where ω_0 is the central lasing frequency. We can then substitute this solution into our original differential equation to acquire a new equation. This equation can then be further simplified by assuming $\left| \frac{\partial^2 E}{\partial t^2} \right| \ll \left| \omega_0 \frac{\partial E^{f,b}}{\partial t} \right|$ and $\left| \frac{\partial^2 E}{\partial z^2} \right| \ll \left| \beta_0 \frac{\partial E^{f,b}}{\partial z} \right|$, and also defining the group velocity of the travelling wave as v_g and including the refractive index of the medium n , which leads us to the following equation:

$$\frac{\pm \partial E^{f,b}(z, \Omega)}{dz} = -j \frac{\Omega}{v_g} E^{f,b}(z, \Omega) - j \frac{\omega_0}{2cn} \chi(z, \omega + \Omega) E^{f,b}(z, \Omega) + \frac{1}{2} \sqrt{\frac{\mu_0 \omega_0}{\beta_0}} J(z, \omega_0 + \Omega) \quad (2.16)$$

We can now perform another transformation out of the frequency domain to get our final time domain equation:

$$\frac{\pm \partial E^{f,b}(z, t)}{\partial t} + \frac{n}{c} \frac{\partial E^{f,b}(z, t)}{\partial t} = \frac{-\alpha_i}{2} E^{f,b}(z, t) - j P^{f,b}(z, t) + F^{f,b}(z, t) \quad (2.17)$$

In this final step, we've created a new term, F , out of what was previously the stochastic current density. This term will be referred to as the spontaneous emission noise. Both this term and the polarization term will need to be described in more detail when working with this equation.

The model introduces a Lorentzian function in order to calculate the spontaneous emission term. This function is related to the broadening effect discussed earlier, as it models the shape linewidth of the spectrum.

$$L_{i,k}(t) = \Gamma \exp(j(\omega_i - \omega_0) - \Gamma t) \quad (2.18)$$

This step introduces two new indices, i and k . The index i allows us to implement the variation in sizes of the QDs. Since we cannot fabricate QDs of perfectly uniform size, we assume we have N groups of differently sized QDs, with dots in group i having a transition frequency of ω_i . For the index k , we divide the laser cavity lengthwise into multiple slices of

length Δz , with each value of k referring to a different slice along the length of the cavity. Here Γ is the dephasing rate for the interband transition ω_i .

We will also need to incorporate a Gaussian distribution, which contributes to the model's description of inhomogeneous gain broadening. As discussed earlier, this effect arises due to the variation in the sizes of the QDs creating a range of transition energies. To manage this, we can introduce a distribution of the possible transition energies in the system.

$$G_i = \frac{1}{A} \exp\left(-4 \ln 2 \frac{(\hbar \omega_i - \hbar \omega_0)^2}{\Delta E^2}\right) \quad (2.19)$$

This expression G_i represents the probability of a QD belonging to size group i , and A acts as a normalization constant.

An expression for the spontaneous emission can be derived using a simple Einstein approach [34]. These spontaneous emissions are random and independent events, so we introduce an extra term for a group of independent complex random processes. Where $\phi_{i,k}^{f,b}(z, t)$ is a uniform uncorrelated expression between 0 and 2π , this term will be $e^{j\phi_{i,k}^{f,b}(z, t)}$, which will then be filtered using the Lorentzian function through a convolution.

$$L_{i,k} \otimes e^{j\phi_{i,k}^{f,b}(z, t)} = \Gamma \int_{-\infty}^t e^{j(\omega_{i,k} - \omega_0)(t-\tau) - \Gamma(t-\tau)} e^{j\phi_{i,k}^{f,b}(z, \tau)} d\tau$$

$$A_{i,k}^{f,b} = e^{j(\omega_{i,k} - \omega_0)\Delta t - \Gamma\Delta t} A_{i,k}^{f,b}(z, t - \Delta t) + \frac{1}{2} \Gamma \Delta t \left[e^{j\phi_{i,k}^{f,b}(z, t)} + e^{j(\omega_{i,k} - \omega_0)\Delta t - \Gamma\Delta t} e^{j\phi_{i,k}^{f,b}(z, t - \Delta t)} \right] \quad (2.20)$$

For the sake of simplicity, we can just write this large convolution expression as A in which case the spontaneous emission term will be:

$$F^{f,b}(z, t) = \frac{1}{\Delta z} \sum_i \sum_k \sqrt{\frac{\hbar \omega_{i,k} \beta_{sp} N_{i,k}(z, t)}{\pi \Gamma \Delta t}} \frac{1}{2 \tau_{i,k}^{sp}} A_{i,k}^{f,b}(z, t) \quad (2.21)$$

This expression introduces a few other new factors to the model. In particular β_{sp} is a term which accounts for the spontaneous emissions into the active lasing region. $N_{i,k}$ is the number of carriers in slice k within a dot of size group i , and $\tau_{i,k}^{sp}$ is the corresponding spontaneous emission

lifetime. These values relate to the other major part of the model, where the carrier population dynamics will be modelled with a series of rate equations described later in this section.

For the polarization term, this model first calculates a series of microscopic polarizations. The microscopic polarization refers to the polarization contributed by each of the N groups of differently sized QDs, and these values can be summed up to find the macroscopic polarization seen in 2.17. This macroscopic polarization can thus be defined as follows:

$$P^{f,b}(z,t) = \sum_i \sum_k p_{i,k}^{f,b}(z,t) \quad (2.22)$$

This expression for the macroscopic polarization can be further defined in terms of the optical susceptibility [15].

$$P^{f,b}(z,t) = \frac{\omega_0}{2cn} \chi(z,t) \otimes E^{f,b}(z,t) \quad (2.23)$$

Combining these two equations, we can create an expression for the microscopic polarization of dot group i .

$$p_{i,k}^{f,b}(z,t) = \Gamma_{xy} \frac{\omega_0 D_k G_i N_d}{2cnH_w \epsilon_0} \frac{j |d_k^i|^2 (2f_{i,k} - 1)}{\hbar \Gamma} L_{i,k}(t) \otimes E^{f,b}(z,t) \quad (2.24)$$

However, we have now introduced several new values as well as another convolution term, this time with the Lorentzian function and the electric field. Γ_{xy} is the mode confinement factor, $d_{i,k}$ is a dipole matrix element, and $f_{i,k}$ is the carrier occupation probability for state k in dot group i . To simplify this and differentiate it from our earlier convolution expression, this term will be referred to as B .

$$L_{i,k} \otimes E^{f,b}(z,t) = \Gamma \int_{-\infty}^t e^{j(\omega_{i,k} - \omega_0)t - \Gamma(t-\tau)} E^{f,b}(z,\tau) d\tau$$

$$B_{i,k}^{f,b} = e^{j(\omega_{i,k} - \omega_0)\Delta t - \Gamma\Delta t} B_{i,k}^{f,b}(z,t - \Delta t) + \frac{1}{2} \Gamma \Delta t \left[E^{f,b}(z,t) + e^{j(\omega_{i,k} - \omega_0)\Delta t - \Gamma\Delta t} E^{f,b}(z,t - \Delta t) \right] \quad (2.25)$$

These equations will describe the evolution of the electric field in time and space, but it relies on the dynamics of the carriers within the system. To properly solve these equations, we will need a second system of rate equations which describe the carrier populations in each energy

level. This system of equations will be similar to very basic model of laser dynamics described in section 2.3, but with some additions.

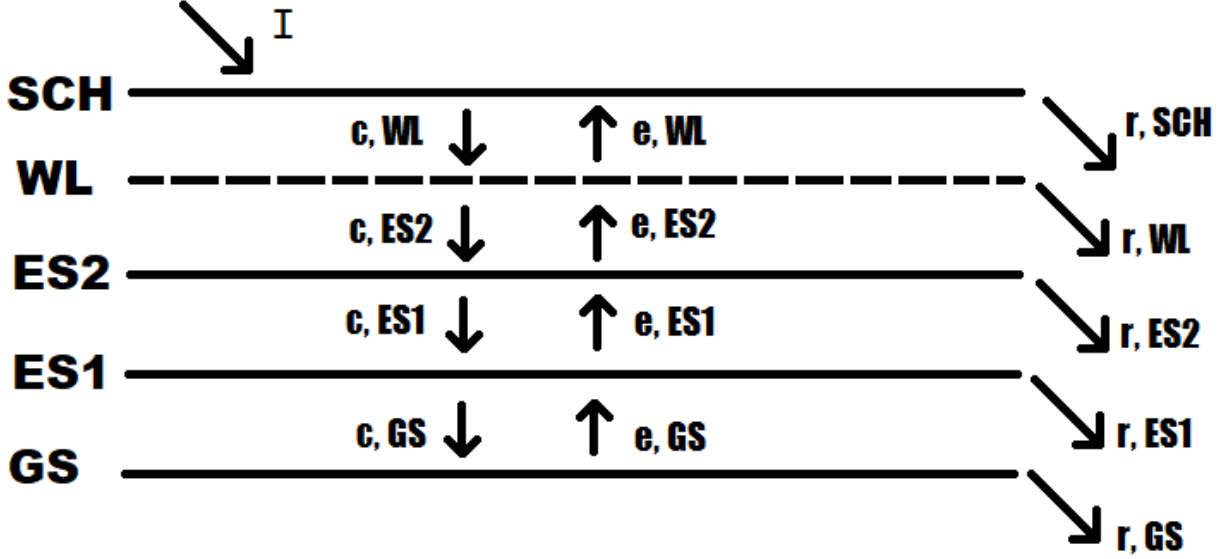


Figure 2.6 Diagram of the energy level diagram used in this model, including all relevant transitions and their lifetimes

Here, we will concern ourselves with five different energy levels: the ground state (GS), two excited states (ES1 and ES2), the wetting layer of the device (WL) and a separate confinement heterostructure (SCH). Lasing will be occurring in the two excited states, with carriers being injected into the SCH and then decaying down from WL into ES2, ES1 and GS, where a population inversion will start to build up.

$$\frac{dN_{SCH}}{dt} = \eta_i \frac{J}{e} \Delta z W - \frac{N_{SCH}}{\tau_r^{SCH}} - \frac{N_{SCH}}{\tau_c^{WL}} + \frac{N_{WL}}{\tau_e^{WL}} \quad (2.26)$$

$$\frac{dN_{WL}}{dt} = \frac{N_{SCH}}{\tau_c^{WL}} - \frac{N_{WL}}{\tau_e^{WL}} - \frac{N_{WL}}{\tau_r^{WL}} - \sum_i \frac{G_i}{\tau_c^{ES2}} N_{WL} (1 - f_{ES2}) + \frac{N_{ES2}}{\tau_e^{ES2}} \quad (2.27)$$

$$\frac{dN_{ES2}}{dt} = \frac{G_i}{\tau_c^{ES2}} N_{WL} (1 - f_{ES2}) - \frac{N_{ES2}}{\tau_e^{ES2}} - \frac{N_{ES2}}{\tau_{sp}^{ES2}} - \frac{N_{ES2}}{\tau_c^{ES1}} (1 - f_{ES2}) + \frac{N_{ES1}}{\tau_e^{ES1}} (1 - f_{ES2}) \quad (2.28)$$

$$\begin{aligned} \frac{dN_{ES1}}{dt} = & \frac{N_{ES1}}{\tau_c^{ES2}}(1 - f_{ES1}) - \frac{N_{ES1}}{\tau_e^{ES1}}(1 - f_{ES2}) - \frac{N_{ES1}}{\tau_s^{GS}} - \frac{N_{ES1}}{\tau_c^{GS}}(1 - f_{GS}) + \frac{N_{GS}}{\tau_e^{GS}}(1 - f_{ES}) - \dots \\ & \dots - \frac{j \Delta z}{\hbar \omega_{i,ES1}} \left[\left(E^f \text{conj}(p_{ES1}^f) - \text{conj}(E^f) p_{ES1}^f \right) + \left(E^b \text{conj}(p_{ES1}^b) - \text{conj}(E^b) p_{ES1}^b \right) \right] \end{aligned} \quad (2.29)$$

$$\begin{aligned} \frac{dN_{GS}}{dt} = & \frac{G_i}{\tau_c^{GS}} N_{WL} (1 - f_{GS}) - \frac{N_{GS}}{\tau_e^{GS}} - \frac{N_{GS}}{\tau_{sp}^{GS}} - \dots \\ & \dots - \frac{j \Delta z}{\hbar \omega_{i,ES1}} \left[\left(E^f \text{conj}(p_{GS}^f) - \text{conj}(E^f) p_{GS}^f \right) + \left(E^b \text{conj}(p_{GS}^b) - \text{conj}(E^b) p_{GS}^b \right) \right] \end{aligned} \quad (2.30)$$

Although the theoretical model describes lasing from two different excited states, most simulations use a simplified version which only looks at lasing from the first excited state, and thus only use four levels. This five level model is presented for completeness, and because this approach is incorporated into the model which the perturbation theory simulation is built around.

These carrier populations are also closely related to the occupation probabilities introduced earlier, through an additional equation:

$$N_{i,k}(z, t) = N_l N_D G_i D_k f_{i,k}(z, t) W \Delta z \quad (2.31)$$

This uses the Gaussian distribution for the different dot sizes, as well as the width of the laser cavity, the total number of carriers N_D , the number of QD layers N_l , and the degeneracy of the given state D_k . These extra values are largely based on the specific parameters used in the simulation.

There are a variety of different lifetimes used in this model. The subscript indicates which kind of transition it describes (escape, recombination, and spontaneous emission) and the superscript indicates the initial state of the carrier before the transition.

The spontaneous emission lifetimes are derived using the same Einstein approach used to derive the spontaneous emission term [34]. The escape can be described using this relationship: [35]

$$\tau_{k_1 \rightarrow k_2} = \tau_{k_2 \rightarrow k_1} e^{\frac{\hbar(\omega_{k_2} - \omega_{k_1})}{k_B t}} \quad (2.32)$$

Both the electric field and the carrier dynamics portions of the models use an iterative approach to solve for the needed values and all necessary points in time and space. With this kind of approach, the value of any function $f(x)$ at $x + \Delta x$ is estimated by taking the value at x and adding $\frac{df}{dx} \Delta x$.

$$f(x + \Delta x) = f(x) + \frac{df}{dx} \Delta x \quad (2.33)$$

This approach is very simple to apply to the population rate equations, but the electric field equation 2.17 will need to be modified further, by converting it back into the time domain. This allows it to work much better with the iterative scheme.

$$E^{f,b}(z \pm \Delta z, t \pm \Delta t) = E^{f,b}(z, t) - jP^{f,b}(z, t) \Delta z + F^{f,b} \Delta z - \frac{\alpha_i}{2} E^{f,b}(z, t) \Delta z \quad (2.34)$$

There are a few limitations involved in this model. For example, though the TDTW approach has some computational advantages, it makes it very difficult to properly incorporate effects such as four-wave mixing, group phase dispersion and self-phase modulation [13]. Four-wave mixing is of particular interest here, and it will need to be incorporated to properly investigate this phenomenon. Therefore, it is necessary to build upon these previous models to improve simulation results.

2.5 Perturbation Theory Model

To get around some of the limitations associated with the TDTW model, a modified treatment of the electric field which more thoroughly integrates the effects of FWM has been developed. In addition to maintaining important details like a non-linear refractive index, spatial hole burning, and first-order Taylor expansions with a central difference approximation [13], this alternative model primarily focuses on an advanced treatment of electron-light interaction using perturbation theory, and the interaction of multiple modes [17].

Chow *et al.* [17] presents a multimode description of the electric field within the laser cavity. By introducing both a term for the phase shift of the n th mode $\varphi_n(t)$ and a passive resonator eigenfunction $u_n(z)$, the solution to our previous differential equation for the electric field may be written as follows:

$$E(z, t) = \frac{1}{2} e^{-j\Omega_0 t} \sum_n E_n(t) e^{-j\phi_n(t)} u_n(z) \quad (2.35)$$

Here, the electric field $E(t)$ is expressed as a superposition of several modes, $E_n(t)$. This model also draws a clear distinction between the frequencies of the photons emitted during certain transitions (ω) and the frequency of the standing waves inside the cavity ($\Omega_n = nc / 2Ln_b$). For simplicity, moving forward this model will focus on a function representing the dimensionless amplitude of the field rather than the full value of the electric field, $\xi = \frac{\varphi E}{2\hbar\gamma}$.

Starting from this simple equation, we can apply the Maxwell-semiconductor-Bloch equations [37] as well as using the slowly varying envelope approximation and then arrive at a reduced wave equation for the electric field amplitude.

$$\frac{d\xi}{dt} = -\gamma_c \xi(t) + j \frac{\omega \Gamma}{\epsilon} P(t) \quad (2.36)$$

This fairly simple wave equation depends largely on the optical mode confinement factor $\Gamma = \frac{N_{QW} WH}{W_f H_f}$, which is defined based on the properties of the gain structure of the laser. This factor looks at the number of quantum well (QW) layers embedded with QDs which act as the active medium as well as the width and height of the active region compared with the width and height of the laser beam. The other important factor here is the macroscopic polarization, which will also depend on position in addition to time. Similar to the previous model, this term we use for the polarization comes from summing up several microscopic polarization contributions. The polarization is important to model the interactions between charged carriers, and by summing up several small polarizations, we can model the aggregate of millions of different interactions with a single equation. This approach lets us model all of the QDs as an active medium, while still treating interactions individually via the microscopic polarization terms which we are summing up.

$$P(t) = \frac{1}{2} e^{-j\omega_0 t} \sum_n P_n(t) e^{-j\phi_n(t)} u_n(z) \quad (2.37)$$

We will further need to derive this expression for the microscopic polarization contributions from individual electron-hole pairs, which is integrated across the length of the whole cavity.

$$P_n(t) = \frac{2\Gamma\delta\omega}{V} \sum_q e^{j\omega_0 t + j\phi_n(t)} \frac{2}{L} \int_0^L u_n(z) p_q(t) dz \quad (2.38)$$

The derivation of the solution for the microscopic polarization terms requires equations of motion found by taking the Hamiltonian of a combined system which includes both electrons and holes [17]. Chow *et al.* have demonstrated that this can be solved using either the Heisenberg or Schrodinger picture of quantum mechanics, and that we can also add a 3rd-order term derived using perturbation theory to provide a description of electron-light interactions.

$$p_q(t) = p_q^{(1)}(t) + p_q^{(3)}(t) \quad (2.39)$$

The microscopic polarization of each relevant energy level is simply the sum of their derived 1st- and 3rd-order contributions.

$$\begin{aligned} p_q^{(1)}(t) &= -j(n_{e,q} + n_{h,q} - 1) \sum_n u_n(z) \xi_n(t) e^{-j\phi_n(t)} D_\gamma(\omega_q - \Omega_n) \quad (2.40) \\ p_q^{(3)}(t) &= 2j(n_{e,q} + n_{h,q} - 1) \sum_{n',m,m'} u_{n'}(z) u_m(t) u_{m'}(t) \xi_{n'}(z) \xi_m(t) \xi_{m'}(t) \dots \\ &\dots e^{-j[\phi_{n'}(t) - \phi_m(t) + \phi_{m'}(t)]} e^{j(\omega_q - \Omega_{n'} + \Omega_m - \Omega_{m'})t + \gamma t} D_\gamma(\Omega_m - \Omega_{m'}) \dots \\ &\dots \frac{\gamma_{ab}}{\gamma} D_\gamma(\omega_q - \Omega_{n'} + \Omega_m - \Omega_{m'}) [D_\gamma(\omega_q - \Omega_m) + D_\gamma(\omega_q - \Omega_{m'})] \quad (2.41) \end{aligned}$$

The third order term uses three different indices, n' , m , m' , as well as the electric field amplitude and a complex Lorentzian function $D_\gamma(x) = (1 + jx/\gamma)^{-1}$ which represents the carrier dispersion in the cavity.

By summing up the solutions for this equation to find the polarization in all relevant energy levels ($q = 1, 2, 3, 4, 5$), we can find an expression for the macroscopic polarization, which can then be used in conjunction with eq. 2.36 to solve for the magnitude of the electric field. This will give us a slowly varying amplitude for each cavity mode, which depends on both the cavity gain and an extra coefficient derived from the 3rd-order term.

$$\frac{d\xi_n}{dt} = \left[g_n^{sat} - \frac{\Omega_0}{2Q} \right] \xi_n(t) - \sum_{n',m,m'} \text{Real}[\Theta_{nn',mm'}] \xi_{n'}(t) \xi_m(t) \xi_{m'}(t) \quad (2.42)$$

This coefficient Θ arises from our third order polarization term and is referred to as the general 3rd-order coefficient. It depends heavily on the population inversion, the density of states within the QDs, and an extra factor which is added to model the effects of spatial hole burning.

$$\Theta_{nn',mm'} = \frac{\Gamma \Omega_0 \wp^2}{2\epsilon \hbar \gamma d} \frac{Y_{ab}}{\gamma} D(\Omega_m - \Omega_{m'}) \sum_q n_q^{inv} \eta_{n',mm'} D(\omega_q - \Omega_{n'} + \Omega_m - \Omega_{m'}) \dots \\ \dots [D(\Omega_m - \omega_q) + D(\omega_q - \Omega_m)] \quad (2.43)$$

To define the population inversion within the system, a function for the carrier distributions must be used. Rather than just focusing on electrons, like in the previous model, this one looks at both electrons (e) and holes (h). In the term here which evaluates the extent of the population inversion in the system, n_q^{inv} , the subscript q indicates in which energy level we are looking at the distribution of electrons and holes.

$$n_q^{inv} = f^{e,q} + f^{h,q} - 1 \quad (2.44)$$

To calculate this, we will need to use additional functions for the distributions of carriers. Many models and other papers have used simple Fermi-Dirac distributions for both holes and electrons, but this isn't ideal as their approach assumes that the system remains in equilibrium which can lead to inaccurate predictions. To help work around this flaw, modified Fermi-Dirac distributions will be used to avoid making any inconvenient assumptions.

$$f^{i,q}(E^{i,q}, \mu^i) = \frac{1}{\exp\left(\frac{E^{i,q} - \mu^i}{kT}\right) + 1} \quad (2.45)$$

This simple distribution revolves around both the temperature T of the system as well as the average energy E and chemical potential μ of carriers on each different energy level q . The main adjustment in this approach comes in the handling of the chemical potential. To avoid the assumption of thermal equilibrium, rather than using a constant value for the average chemical potential it will be a function which depends on the varying populations in the ground state [18].

$$N_0 = N_{qw} N_{qd} f^{i,0}(E^{0,i}, \mu^i) \quad (2.46)$$

This equation looks at the initial conditions of the system, before the pump is applied. Prior to any excitations, the number of carriers in the lowest level N_0 must be equal to the total number of carriers in the system (the number of QW layers N_{qw} times the number of dots per layer N_{qd}). Prior to the pumping the system will also be in equilibrium, meaning we can use a Fermi distribution at this instant. By rearranging this, we can find an expression for the varying chemical potential after the pumping has begun as a function of the current population within the ground state.

$$\mu^i = E^{0,i} - kT \ln \left(\frac{N_{qw} N_{qd}}{N_0} - 1 \right) \quad (2.47)$$

By using this modified function for the chemical potential with a basic Fermi distribution, we now have a better picture of the population inversion in the system in non-equilibrium conditions. In addition to the inversion's role in the 3rd-order coefficient and the rate equation for the electric field, we will also need to define the electronic density of states. As discussed earlier, the ideal picture for the energy bands in a QD would be a delta function. In reality, however, we will end up with significant broadening. In an attempt to incorporate this inhomogeneous gain broadening, we can represent the density of states using a simple Gaussian distribution.

$$D(E) = \frac{2 N_{QD}}{\sqrt{2\pi} \Delta_{inh}} e^{-\left(\frac{E}{\sqrt{2}\Delta_{inh}}\right)^2} \quad (2.48)$$

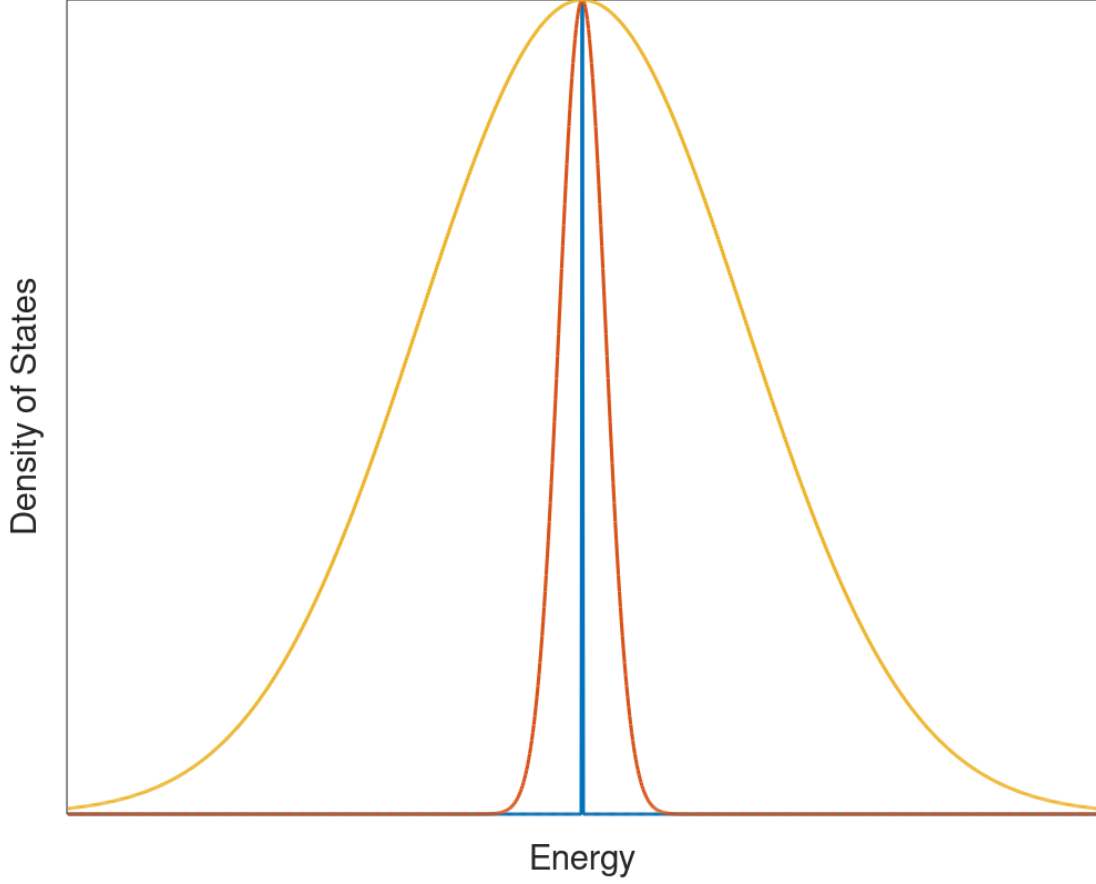


Figure 2.7 Diagram showing how the electronic density of states is modelled using a Gaussian function based on the inhomogeneous broadening effect, illustrating the broadening as Δ_{inh} increases

Another important term which enters the model through the 3rd-order coefficient Θ is the effect of spatial hole burning. This term approximates the effects that arise from the diffusion of carriers caused by what is referred to as Riskan-Nummndal-Graham-Haken (RNGH) instability [21]. These instabilities typically arise from interactions with a saturable absorber [38][39], but since this model is focusing on single section lasers, they will likely not be a factor in any SHB which occurs. Instead, we will focus on a more simple treatment of SHB.

$$\eta_{m,n} = \frac{1}{8} \left[1 + \frac{2}{L} \int_0^L \left(\cos \frac{2\pi(m-n)z}{L} + \cos \frac{2\pi(m-n)z}{L} \right) dz \right] \quad (2.49)$$

Starting from eq. 2.49 we integrate across the length of the entire cavity, we end up with a fairly simple expression which we can incorporate into the model.

$$\eta_{n,m} = \frac{1}{8} + \frac{\sin[2\pi(m-n)]}{4\pi(m-n)} \quad (2.50)$$

The gain is one of the other important elements of the rate equation for the field amplitude. A_n and $B_{n,m}$ are coefficients relating to gain saturation, both self-saturation within a single mode (A_n), and cross saturation between different modes ($B_{n,m}$). These forms of saturation both modify the gain of the cavity. This variation of the gain as the modes saturate and desaturate is similar to the gain-loss cycle seen in two-section lasers, as shown in Figure 1.3. The expressions for both the cross and self-saturation effects can be expressed in terms of the complex 3rd-order coefficient Θ .

$$A_n = \frac{\text{Real}(\Theta_{nnnn})}{g_n} \quad (2.51)$$

$$B_{n,m} = \frac{\text{Real}(\Theta_{nnmm} + \Theta_{mmnn})}{g_n} \quad (2.52)$$

Both of these saturation terms act to modify the gain, such that when they grow the gain decreases and vice versa. As maintaining a large population inversion is the primary means of releasing energy in the laser, the power and thus the linear gain of the system is defined in terms of the population inversion term.

$$g_n = \text{Real}\left(\frac{\Gamma \Omega_0 \wp^2}{2\epsilon \hbar \gamma d} \sum_q n_q^{\text{inv}} D_\gamma(\Omega_n - \omega_q)\right) \quad (2.53)$$

$$g_n^{\text{sat}} = \frac{g_n}{1 + A_n \xi_n^2 + \sum_{m \neq n} B_{n,m} \xi_m^2} \quad (2.54)$$

Here the gain relies heavily on the carrier dispersion, which uses the same complex Lorentzian function from the microscopic polarization equations. The passive cavity is also saturated during this process, leading to saturation of the passive cavity frequency as follows:

$$\Omega_n^{\text{sat}} = \Omega_n + \sigma_n - \tau_n \xi_n^2 - \sum_{m \neq n} \tau_{n,m} \xi_m^2 \quad (2.55)$$

From here, just like in the TDTW model, after the electric field and the polarization are defined, we will need rate equations for the carrier populations in each energy level. This model will use a five-level approach very similar to the one used in the TDTW model. Here we will define five energy levels, N_1 , N_2 , N_3 , N_4 , and N_5 , which will take the place of N_{GS} , N_{ES1} , N_{ES2} , N_{WL} , and N_{SCH} in a series of rate equations based on equations 2.26-2.30, only without the addition of the dot size distributions and complex conjugates. Unlike the simulations based around the TDTW model, we will also be using rate equations for five energy levels, rather than only four.

$$\frac{dN_5}{dt} = \eta \frac{J}{q} LW - \frac{N_5}{\tau_{r5}} - \frac{N_5}{\tau_{c4}} + \frac{N_4}{\tau_{e4}} \quad (2.56)$$

$$\frac{dN_4}{dt} = \frac{N_5}{\tau_{c4}} - \frac{N_4}{\tau_{e4}} - \frac{N_4}{\tau_{r4}} - \frac{N_4}{\tau_{c3}}(1 - f^{e,3}) + \frac{N_3}{\tau_{e3}} \quad (2.57)$$

$$\frac{dN_3}{dt} = \frac{N_4}{\tau_{c3}}(1 - f^{e,3}) - \frac{N_3}{\tau_{e3}} - \frac{N_3}{\tau_{sp3}} - \frac{N_3}{\tau_{c3}}(1 - f^{e,3}) + \frac{N_2}{\tau_{e2}}(1 - f^{e,3}) \quad (2.59)$$

$$\frac{dN_2}{dt} = \frac{N_3}{\tau_{c3}}(1 - f^{e,2}) - \frac{N_2}{\tau_{e2}}(1 - f^{e,3}) - \frac{N_2}{\tau_{sp1}} - \frac{N_2}{\tau_{c1}}(1 - f^{e,1}) + \frac{N_1}{\tau_{e1}}(1 - f^{e,2}) \quad (2.59)$$

$$\frac{dN_1}{dt} = \frac{N_4}{\tau_{c1}}(1 - f^{e,1}) - \frac{N_1}{\tau_{e1}} - \frac{N_1}{\tau_{sp1}} \quad (2.60)$$

In using these equations from the TDTW model, we are also able to bring in the new carrier distributions defined in equation 2.45 along with the varying chemical potential in equation 2.47. The most important part of this portion of the model is the decay rates for each energy level. We will need to calculate the average time for carriers to transition down from a higher level down to a lower one, which is accomplished in the same way as in the previous model, using equation 2.32.

With all of these extra equations and expressions, we finally have all of the information needed to solve the groups of rate equations we need: First the populations dynamics, and then the electric field amplitude. These systems of equations should give us all of the information needed to paint an accurate picture of the working of the laser while better representing the contributions of four-wave mixing.

Chapter 3 – Simulation Details

3.1 Introduction

The perturbation theory-based model described in chapter 2.5 has been recreated using COMSOL Multiphysics 5.4, allowing the modelling of various QD laser devices. COMSOL was chosen over similar software like MATLAB as it simplifies incorporating the geometry of the system, allows us to use a series of constants and functions to represent all the relevant values, and lets us use a connected series of grouped differential equations that will be solved simultaneously. COMSOL also allow for simulations with a much more modular design, which is very useful for models like this which incorporate multiple separate parts. However, though it has many advantages when dealing with systems like this, it doesn't have many tools for mathematical analysis, so MATLAB was also used in order to better process and analyze all of the results from the COMSOL file.

This chapter will outline in detail how all of the elements of the theoretical model were introduced into a single COMSOL program, as well as provide an explanation of some of the rationale behind the choices which were made. There will also be an explanation of the external MATLAB code which was used to process the output data from this simulation and create multiple important figures, and explanation of what it does and how it was used.

3.2 Geometry

The simulation was built on a 3D geometry modelled after a QD embedded in stacked layers on a thick substrate, complete with the thinner wetting layer and capping layer. The QD itself is embedded inside the wetting layer. A diagram of this arrangement is shown in Figure 3.1.

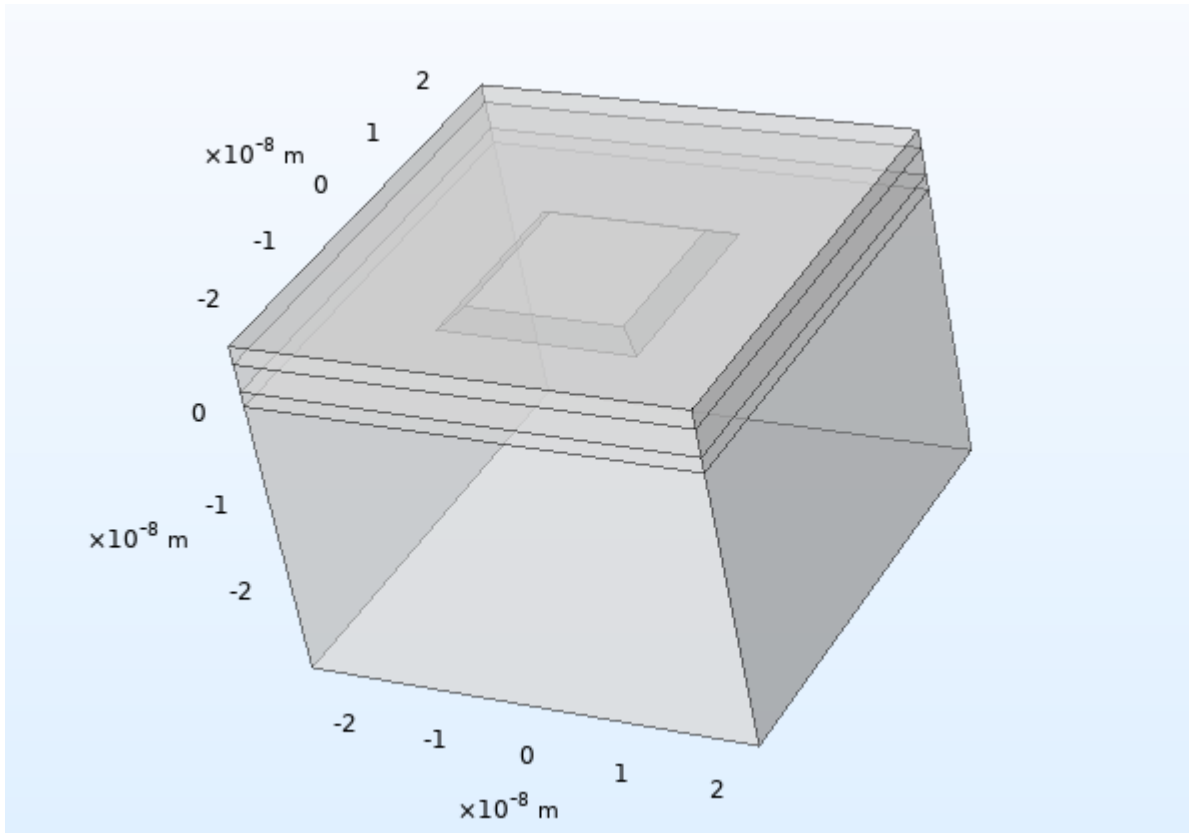


Figure 3.1 Image of the QD geometry, as shown within the simulation

This geometry consists of four main entities: the substrate, the wetting layer, the capping layer (represented by blocks stacked on top of each other) and the dot itself (represented by a pyramid, which rests on top of the wetting layer and is embedded within the wetting layer).

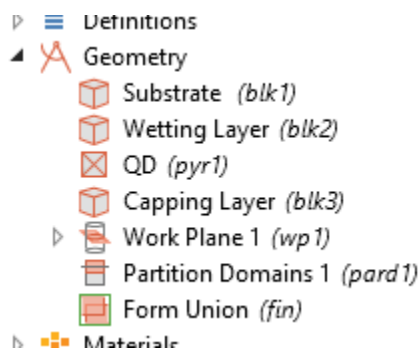


Figure 3.2 Image of the entities included in the model's geometry

The material properties of each portion was modified based on the properties of the device being simulated, but the physical dimensions of the geometry were defined using a series of defined constants.

Table 3.1 Physical dimensions used to define the geometry of the QDs

Parameter Name	Value	Description
H_qd	1.5 nm	QD height
L_outer	48 nm	Length of outer boundary
L_base	11.213 nm	Length of base
T_wet	1.6357 nm	Thickness of wetting layer
T_sub	30 nm	Thickness of substrate

3.3 Functions

Many of the key components of this simulation, such as the carrier distributions, gain coefficients, and SHB factor are all handled using functions within COMSOL. In particular, both the band energies and the transition energies were handled using a table of values listing the energy level for each state.

These values will depend on which material is being used, and as devices using two different kinds of QDs were simulated here, two separate tables of values were used. All of these values were taken from published measurements from the same types of QDs being simulated [26][27].

Table 3.2 Carrier energies and transition energy values for InGaAs/GaAs QDs [26]

Energy Level (q)	Electron energy (eV)	Hole energy (eV)	Recombination energy (eV)
1	0.75	-0.54	1.30
2	0.78	-0.54	1.33
3	0.78	-0.55	1.34
4	0.79	-0.55	1.35

Table 3.3 Carrier energies and transition energy values for InAs/InP QDs [27]

Energy Level (q)	Electron energy (eV)	Hole energy (eV)	Recombination energy (eV)
1	2.124	1.287	0.837
2	2.432	1.580	0.852
3	2.432	1.561	0.871
4	2.442	1.537	0.905

The energies for the InGaAs/GaAs are taken directly from [26], but the published results from [27] needed to be adapted a bit to fit this model's approach to the energy levels and recombination energies for the InAs/InP QD lasers. As this model treats the transition down from level 3 to level 2 as the primary radiative transition, this will be assigned the energy measured for the p-shell transition, as it is the dominant transition. The other observed transitions, including the s-shell, are assigned accordingly relative to their position in the spectrum, and the electron and hole energies were extrapolated based on the recombination energies and the electron state energies reported by Franceschetti *et al.* [40]

In a similar fashion, the term for the SHB will be treated using a piecewise function which takes one argument rather than two. This is the term described in equation 2.50. The use of a single argument ($m - n$) rather than two (m and n) is for the sake of simplicity, but the choice to use a piece-wise function for what would otherwise be a continuous function is because in cases of self-saturation, where $m = n$, we will end up dividing by 0.

To avoid this issue, a function with three pieces is used. For the first two portions of the domain, $m - n < 0$ and $m - n > 0$, we simply calculate the expression as shown in equation 2.50, but for very small values of $m - n$ (between -0.01 and 0.01) we instead use an approximation to avoid dividing by zero. For very small values of x , we can say $\sin(x) \approx x$, which means we can approximate $\sin[2\pi(m - n)] \approx 2\pi(m - n)$, and further simplify the SHB expression. Using this approximation, we can then create a new expression for the SHB for very small mode differences which will allow us to avoid having to divide by zero.

$$\eta_{n,m} \approx \frac{1}{8} + \frac{2\pi(m-n)}{4\pi(m-n)}$$

$$\eta_{n,m} \approx \frac{1}{8} + \frac{1}{2}$$

$$\eta_{n,m} \approx \frac{5}{8}$$

Argument:	x	
Extrapolation:	None	
Smoothing:	Continuous first derivative	
Transition zone:	Relative size	
Size of transition zone:	0.1	
— Intervals —		
» Start	End	Function
-m2	-0.01	1/8+sin(2*pi*x)/(4*pi*x)
-0.01	0.01	5/8
0.01	m2	1/8+sin(2*pi*x)/(4*pi*x)

Figure 3.3 The piece-wise function used to model the effects of spectral hole burning

Other than these exceptions, the other important coefficients were simply calculated using simple analytic functions. In total, ten of these analytic functions were used: density of states (2.48), the Lorentzian dispersion function, cavity mode frequencies, chemical potential for electrons, chemical potential for holes (2.47), population inversion (2.44 and 2.45), the general 3rd-order coefficient (2.43), self-saturation (2.51), and cross-saturation (2.52). All of these functions were represented exactly as outlined in the relevant passages of section 2.5.

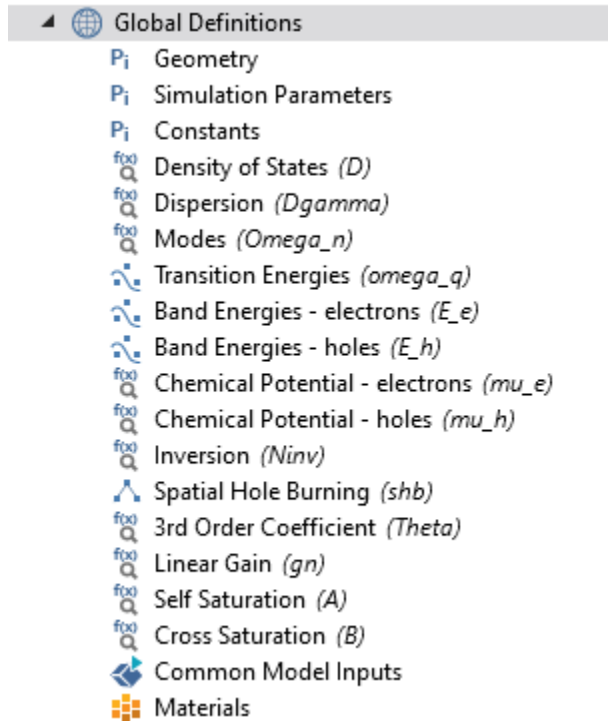


Figure 3.4 Image of the functions used to calculate the important variables in this model

All of these functions refer to each other in some capacity, such as using output from other functions as an input argument, but they also interact with the systems of differential equations described in the next section.

However, these differential equations are not defined globally, so the key variables are not available to be used by other functions and operation within the simulation. For example, the chemical potentials both depend on the population in the ground state of the system. As this is not a globally available variable, it cannot be used in the calculation. To work around this, any functions that depend on the population of the ground state N_1 are set up so that in addition to the necessary arguments they also take the population in the ground state of the QDs. This way whenever these values are used, the differential equation part of the model can simply pass the current value of the relevant variable to the function.

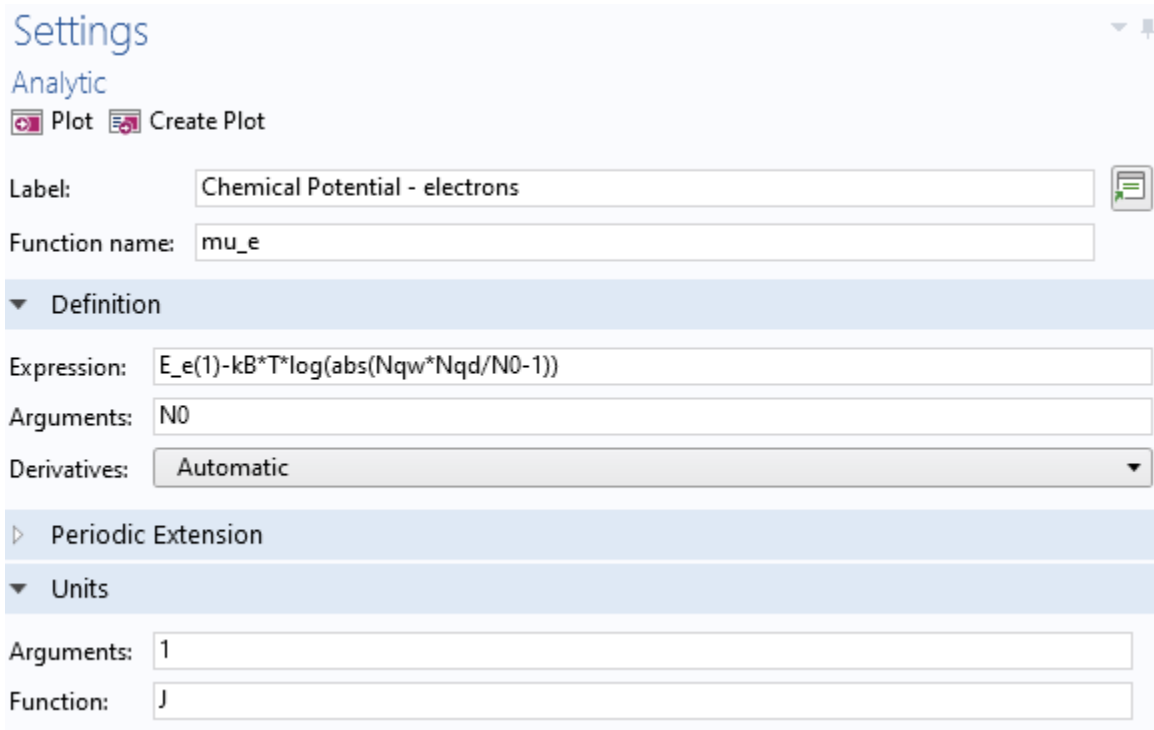


Figure 3.5 The function for the chemical potential for electrons, illustrating how globally inaccessible variables are included as arguments

All of these functions are closely connected to each other, with some of them being composites of some of these other functions. All of these functions will be needed to solve the main backbone of the model: the time domain differential equations describing the carrier populations and the electric field magnitude.

3.4 Differential Equations

This program uses multiple systems of equations to calculate the two main parts of this model: the carrier populations and the electric field magnitude. All three of these differential equations use separate Domain ODEs and DAEs (**dode**) physics modules, with all of them operating within the QD within the geometry. In the case of the electric field, only a single dependent variable is used for each, but since the population model has equations for each energy level we will need to set up the module with five different dependent variables (N_1 , N_2 , N_3 , N_4 , and N_5).

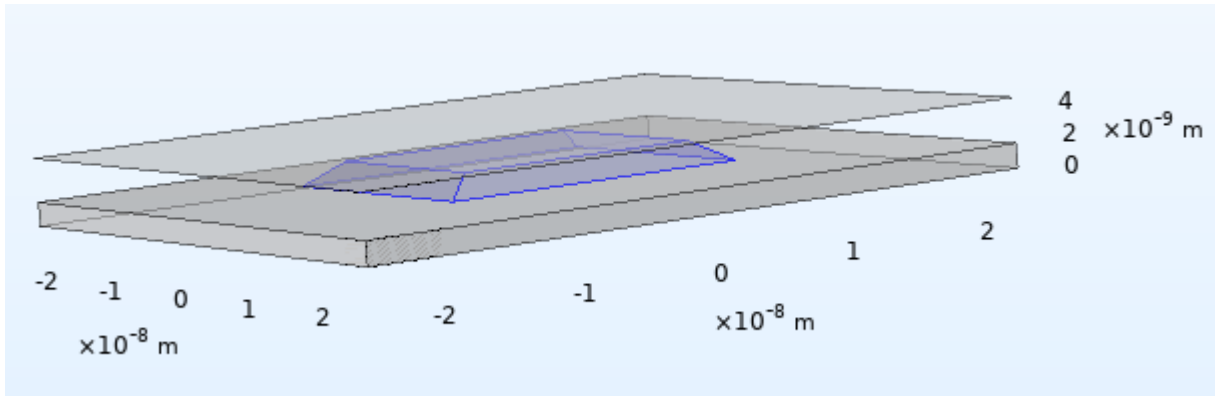


Figure 3.6 Diagram of the domain on which all three domain ODEs are calculated

The Domain ODEs and DAEs physics modules all use the same general form, where \mathbf{u} is a vector containing each of the dependent variables, and e_a and d_a are coefficient matrices referred to as the mass coefficient and the damping coefficient, respectively.

$$e_a \frac{\partial^2 u}{\partial t^2} + d_a \frac{\partial u}{\partial t} = f \quad (3.1)$$

As none of our differential equations involve second order derivatives, e_a will simply be 0 in all cases, and since all of our equations are formatted as simple first order differential equations, while d_a will simply be 1 (or the identity matrix in the case of the populations).

All four components of the variable f will be the time derivatives of N_1 , N_2 , N_3 , N_4 , and N_5 , exactly as defined in 2.56-2.60. This simulation also adds a series of restrictions in order to maintain carrier conservation. Through multiple constraints, it is set up so that both the total number of carriers in the system remains constant and so that each of the individual populations remains positive.

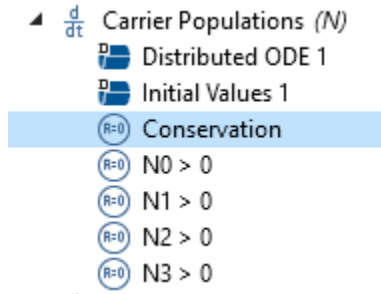


Figure 3.7 Image of the constraints set up to maintain conservation in the carrier rate equations

For the first conservation constraint, we focus on the total number of carriers in the system. We use the parameter N_{QD} , which describes the number of carriers in the system and is set as the initial condition of N_1 . The constraint is set up so that if we subtract all of populations in each level from the total population it will be equal 0. This way, the sum of the populations in each level will always be equal to the total number of carriers in the system.

$$N_{QD} - N_1 - N_2 - N_3 - N_4 - N_5 = 0 \quad (3.2)$$

The other constraints ensure that the populations of each level stay positive by comparing the value for each population with the its absolute value. If N_i has a negative value, than subtracting it will leave you with a large positive values rather than 0, thus violating the constraint.

$$|N_i| - N_i = 0 \quad (3.3)$$

Finally, the last ordinary differential equation to deal with the magnitude of the electric field is handled in a much more straightforward manner. This will only feature a single equation based on equation 2.42, and will take on a very small initial values to spur initial growth.

One additional modification is also required, as equation 2.42 only calculates the electric field of a single mode, we will make use of the `sum()` function in COMSOL to sum up the solutions for the electric field contributions from each mode and leave us with a full expression for the electric field magnitude. This is the portion of the model which takes into account both the self-saturation and cross-saturation of modes as well as all the values for the 3rd-order coefficient, so summing up the terms for each mode from m_1 to m_2 becomes necessary.

```

Source Term
f sum((gn(i,N1)/(1+A(i,N1)*E^2+sum(B(i,j,N1),j,m1,m2)*E^2)-Omega0/2/Q)*E,i,m1,m2)-sum(sum(sum(sum(real(Theta(l,m,i) 1/s

```

Figure 3.8 Demonstration of the use of the sum() function to add up the saturation of each mode

3.5 Parameters

This model requires a large list of important parameters related to the functions and differential equations. Many of these are dependent on the specific device being modelled, but there are some which are used across all simulations. First, however, there are a few universal constants which need to be defined.

Table 3.4 List of all important constants used within the model

Name	Expression	Value	Description
hbar	h_const/2/pi[rad]	1.0546×10^{34} J·s/rad	Reduced Planck Constant
NA	N_A_const	6.0221×10^{23} 1/mol	Avogadro's Constant
q	e_const	1.6022×10^{-19} C	Electron Charge
epsilon0	epsilon0_const	8.88542×10^{-12} F/m	Vacuum Permittivity
kB	k_B_const	1.3806×10^{-13} J/K	Boltzmann's Constant

The remaining important parameters are values related to the equations we have set up for the model, while others are related to properties of the device and the material and optical properties of the dots. The latter parameters will vary in each simulation, and will be outlined later, but some of these values will be the same in each simulation.

Table 3.5 List of all parameters which are used in all versions of the model

Name	Expression	Value	Description
t_step	0.05[ps]	5×10^{-14} s	Time Step
t_start	0[s]	0 s	Start Time
t_end	100[ps]	1×10^{-10} s	End Time
m1	1999	1999	First Mode
m2	2001	2001	Last Mode
eta	0.55	0.55	Carrier Injection Efficiency
inh	10[meV]	1.6022×10^{-21} J	Inhomogeneous Gain Broadening

The values for initial and final time as well as the time step are incorporated into the time dependent solver used to find solutions to the differential equations. Though these time values are used for most of the simulations in order to collect a large amount of data with minimal computation time, some adjustments will be in order to replicate specific time ranges from the published data. These values will always be chosen so that 2000 steps in total are calculated. The rest of these values are all used within the defined functions or differential equations in some capacity.

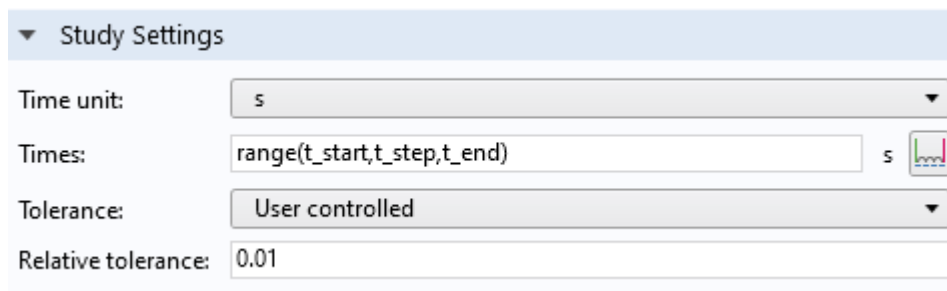


Figure 3.9 The time dependent step set up to solve the domain ordinary differential equations

3.6 Post-Processing

After the simulation has finished running, we can very easily export tables of values for the populations and the electric field, as well as make figures with them. Though COMSOL's built in graphing capabilities are sufficient for basic plots of these values, for a more detailed

analysis of the results we turn to MATLAB. After exporting these data tables as .txt files, they can very easily be imported into MATLAB and used as data. From here, they are entered into a program which processes this data to generate multiple additional figures, such as the gain spectrum of the laser.

There are two different programs here which use different approaches, one focusing on the electric field and the other on the populations. The first starts by isolating the last nine tenths of the calculated electric field values and stored them in a new variable. By ignoring the first few values, we ignore the initial activity from switching on the laser and instead focus on the pulsing behaviour of the laser.

In both cases, once we have isolated a short portion of the time domain activity of the electric field, a frequency domain Fast Fourier Transform (FFT) is performed on this segment of the electric field to convert these values into the frequency domain. Using an understanding of the basic properties of waves, this can also provide us with values in the wavelength domain. We can then also use the `fftshift()` function to centre the zero-frequency component at the centre of our gain spectrum. These values can then be used to calculate the absolute gain across the entire spectrum in dBm.

$$F_{dBm} = 10 \log \left(\frac{F}{\bar{F}} \right) \quad (3.4)$$

The code then creates another variable to store a version of the gain spectrum which has been normalized. This is achieved simply by taking the original spectrum and subtracting the maximum value. MATLAB's `pwelch()` function, which applies Welch's power spectral density estimate, is also used to create a frequency domain spectrum measured in dB. The next step of this analysis is to calculate the power of the laser based on the original electric field measurements. This is done simply by multiplying the electric field by its complex conjugate.

Now that all of the data has been fully processed, nine different figures are generated: two plots laser intensity vs time over different time scales, three different figures of wavelength vs dBm for three different spectral ranges, wavelength vs the normalized optical spectrum, two different figures of frequency vs dB, and frequency vs the normalized optical spectrum.

The second program processes the electric field data in the same way, but it obtains this data in a different way. Rather than using the electric field data directly from the simulation, the carrier population data is used. In particular, N_2 and N_3 are focused on, as they take the place of N_{GS} and N_{ES} as described in the old Bardella *et al.* model. Similar to what is described in section 2.4, the program runs through each value of the populations in the time domain and uses them to calculate the occupation probabilities, the spontaneous emission noise terms, and from there calculate the electric field.

Once we have gone through all of these steps to recalculate a collection of values for the electric field, the exact same procedure used in the first program is then carried out using the new electric field values, and the exact same figures are produced.

Both of the programs used here are reproduced in full in the Appendix.

Chapter 4 – Examination of the Proposed Perturbation Theory Model

4.1 Introduction

Several sets of data have been generated using this COMSOL simulation in order to verify the accuracy of the model and its underlying theoretical assumptions. The different sets of published results were picked to illustrate different important properties expected of a QD laser.

The first set of reproductions focuses on RF spectra published by Bardella *et al.* [14] including both data from their TDTW model [15][16] and experimental data. Using the same set of parameters described in the paper, both sets of results were replicated using the new improved model to demonstrate an approximate equivalence between the two approaches and show areas where the new may be an improvement.

In addition to comparing this work to simulations based on the TDTW model, agreement with experimental results is also taken into consideration. Next, a laser studied by Tierno *et al.* [19] is replicated using the perturbation theory simulation and all relevant parameters described in the paper to see how well it can demonstrate the time-domain pulsing behaviour which is one of the most prominent expected features of a mode-locked laser.

Finally, optical spectra from another mode-locked laser published by Majid *et al.* [20] will be recreated by running the same parameters through the simulation. Of particular interest here are the presence of lasing from two peaks and the broadening of those peaks within the spectrum.

4.2 RF Spectra

The first set of results which were replicated were published by Bardella *et al.* to study RF line width and RIN in a single section passively mode-locked laser [14]. The publication involves two sets of spectra: simulated results from a InAs/InGaAs QD laser with a 250 μm long cavity, and experimental results from a InAs/InGaAs QD laser with a 1 mm long cavity. The researchers observe that the lasers start to exhibit mode-locking behaviour after increasing the injection current past a certain point. These results are reproduced in Figure 4.1.

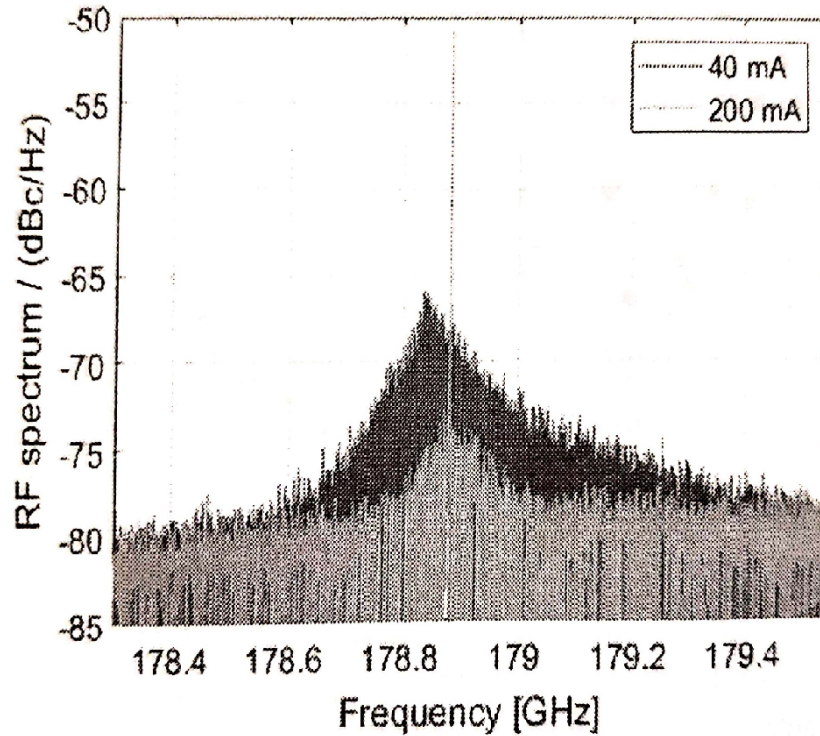


Figure 4.1 RF beat note spectra for a 250 μm long InAs/InGaAs QD laser, from published TDTW simulation results [14]

In addition to the simulated results produced using their TDTW model, some experimental data is also studied in this paper, which shall also be taken into account here. In this case, the actual device is the same as the simulated one in all properties except the cavity length. Once again, the lasing behaviour only becomes evident past a certain current threshold, with a very high power peak only being evident in the spectrum when using a higher injection current. This data is reproduced in Figure 4.2.

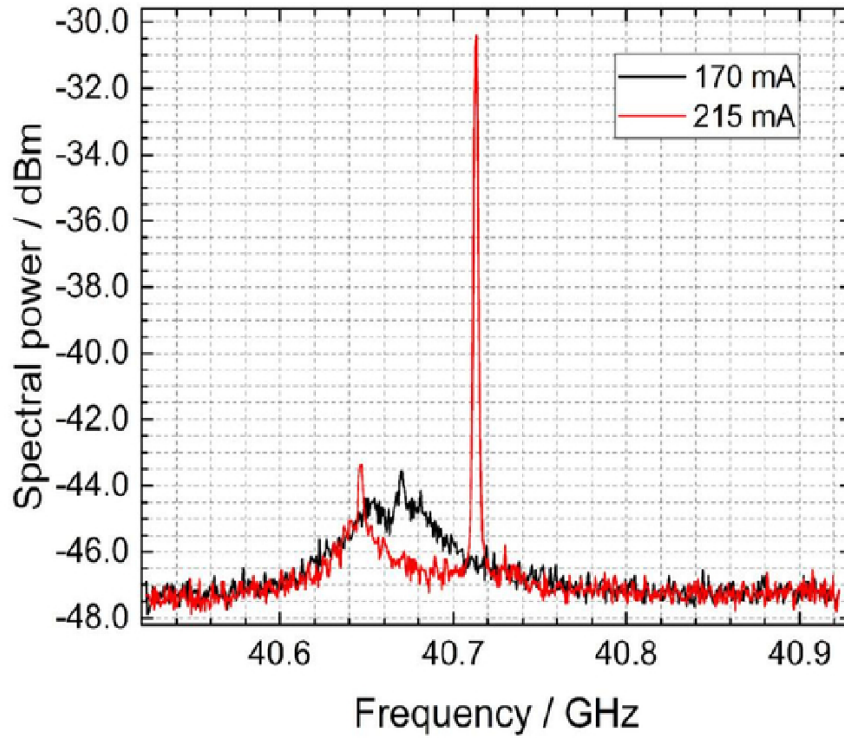


Figure 4.2 RF beat note spectra for a 1 mm long InAs/InGaAs QD laser, from published experimental results [14]

Both the simulation and the experimental results have been reproduced using all of the parameters described in the paper. Almost all of the values needed for the simulation were provided in a table or in the text of the paper, and the rest could be extrapolated or estimated based on given information. These values have been reproduced in Table 4.1.

Table 4.1 List of specific parameters used to simulate results published by Bardella *et al.* [14]

Name	Expression	Value	Description
nb	3.34	3.34	Effective Refractive Index
Nqw	15	15	Number of QW Layers
Nd	$2.7 \times 10^{10} [1/\text{cm}^2]$	$2.7 \times 10^{14} 1/\text{m}^2$	QD Surface Density
dip	$0.72 [\text{eV} \cdot \text{nm}]$	$1.1536 \times 10^{-28} \text{ kg} \cdot \text{m}^3/\text{s}^2$	Dipole Matrix Element
T	283[K]	283 K	Temperature
L	250[um] / 1[mm]	$2.5 \times 10^{-4} \text{ m} / 0.001 \text{ m}$	Cavity Length
W	5[um]	$5 \times 10^{-6} \text{ m}$	Ridge Width
H	5[nm]	$5 \times 10^{-9} \text{ m}$	QD Layer Height
lam0	1250[nm]	$1.25 \times 10^{-6} \text{ m}$	Central Lasing Frequency
I	40[mA], 200[mA] / 170[mA], 215[mA]	0.04 A, 0.2 A / 0.17 A, 0.215 A	Laser Injection Current

The perturbation theory simulation was run four different times, with injection currents and cavity lengths varying in accordance to what was published in an attempt to match these same published results. Plots of the data generated by the simulation are reproduced in Figures 4.3 and 4.4.

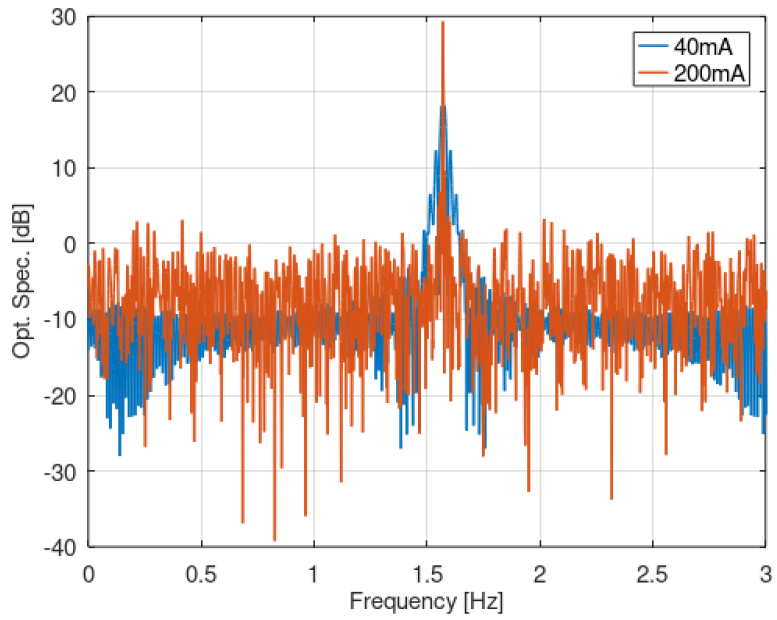


Figure 4.3 RF beat note spectra for a 250 μm long InAs/InGaAs QD laser, from perturbation theory simulation

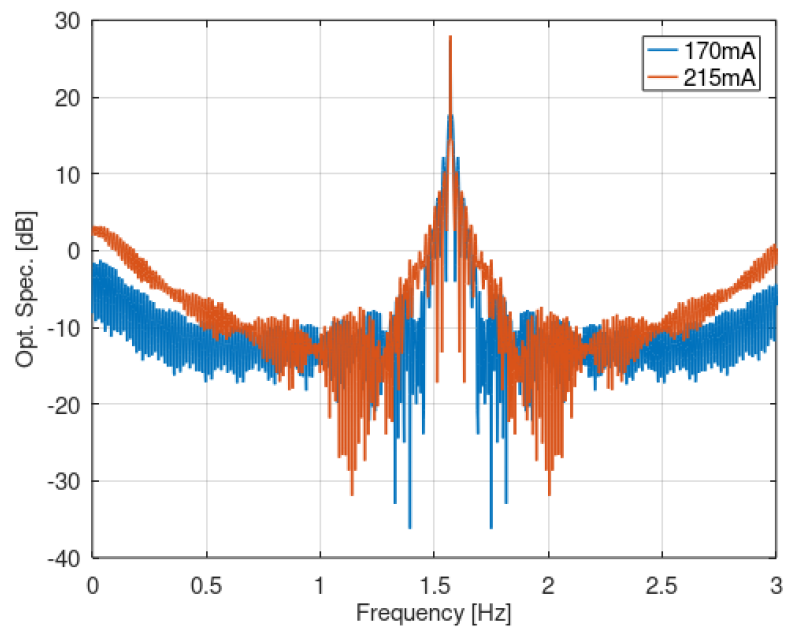


Figure 4.4 RF beat note spectra for a 1 mm long InAs/InGaAs QD laser, from perturbation theory simulation

4.3 Time-Domain Pulses

The next results come from a study of temperature stability in QD lasers published by Tierno *et al.* [19] The authors observe very clear pulsing behaviour in an InAs QD laser over a wide range of injection currents, and the observed periodic pulsing suggests a relationship between the injection current and the period of the gain cycling. This is of particular interest given our focus on mode-locking and how FWM contributes to it. Their published data is reproduced in Figure 4.5.

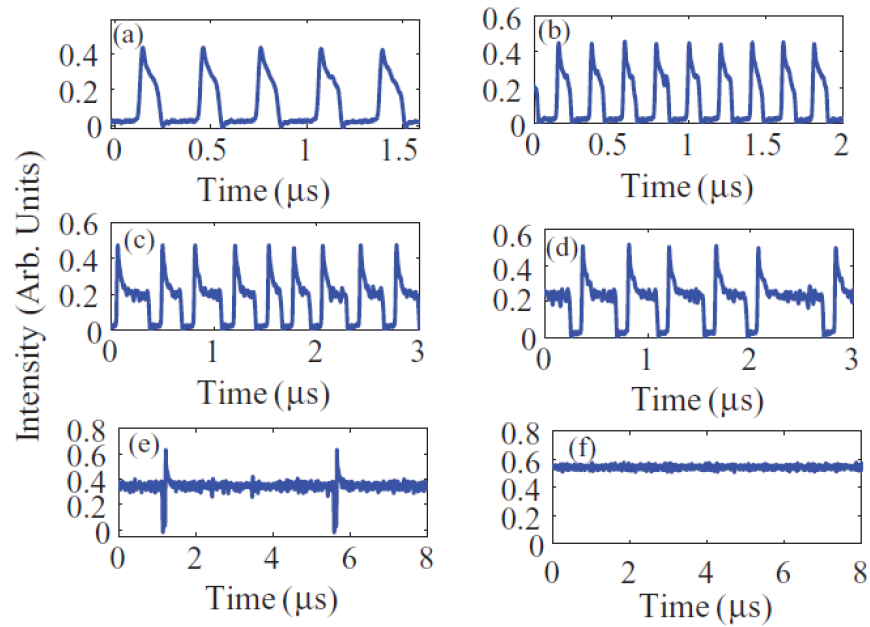


Figure 4.5 Time domain electric field behaviour in an InAs QD laser using an injection current of a) 803 mA, b) 827 mA, c) 832 mA, d) 840 mA, e) 872 mA, and f) 910 mA, from published results [19]

The parameters of the device were all included within the published literature, and the relevant values have been reproduced in Table 4.2. Six different data sets were produced with the perturbation theory model, using injection currents ranging from 803 mA to 910 mA along with different time scales because of the changing repetition rate of the pulses seen in the experimental data. These results are reproduced in Figure 4.6.

Table 4.2 List of specific parameters used to simulate results published by Tierno *et al.* [19]

Name	Expression	Value	Description
nb	3.34	3.34	Effective Refractive Index
Nqw	10	10	Number of QW Layers
Nd	$2.7 \times 10^{10} [1/\text{cm}^2]$	$2.7 \times 10^{14} 1/\text{m}^2$	QD Surface Density
dip	$0.72 [\text{eV} \cdot \text{nm}]$	$1.1536 \times 10^{-28} \text{ kg} \cdot \text{m}^3/\text{s}^2$	Dipole Matrix Element
T	283[K]	283 K	Temperature
L	3.5[mm]	0.0035 m	Cavity Length
W	4.5[um]	4.5×10^{-6} m	Ridge Width
H	5[nm]	5×10^{-9} m	QD Layer Height
lam0	1225[nm]	1.225×10^{-6} m	Central Lasing Frequency
I	803[mA] / 827[mA] / 832[mA] / 840[mA] / 872[mA] / 910[mA]	0.803 A / 0.827 A / 0.832 A / 0.840 A / 0.872 A / 0.910 A	Laser Injection Current

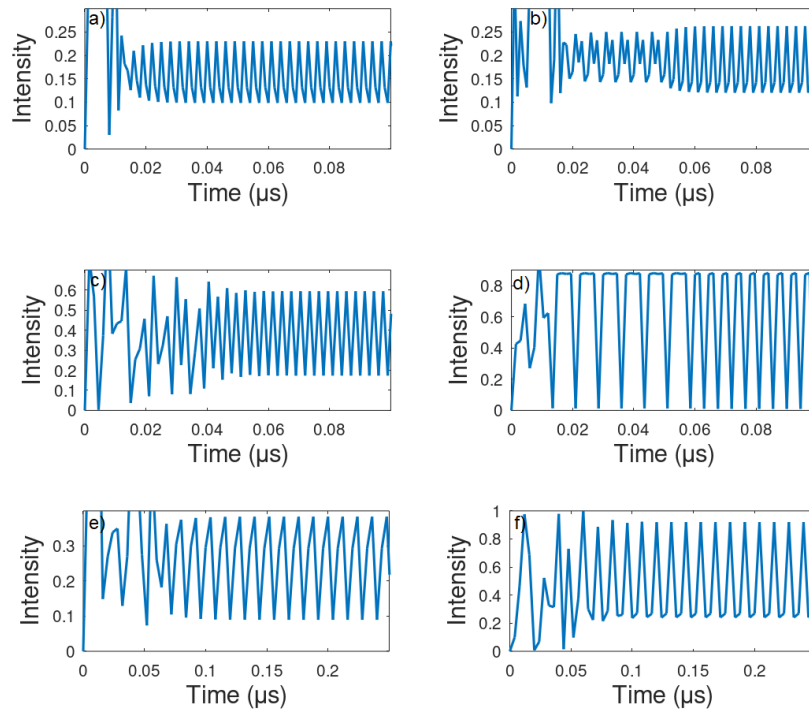


Figure 4.6 Time domain electric field behaviour in a InAs QD laser using an injection current of a) 803 mA, b) 827 mA, c) 832 mA, d) 840 mA, e) 872 mA, and f) 910 mA, from perturbation theory simulation

4.4 Optical Spectrum

Finally, results describing an InAs/GaAs-based passively mode-locked QD laser, from a paper published by Majid *et al.* [20], were reproduced. Of particular interest with these results is the occurrence of lasing at two separate wavelengths, and how the power spectrum evolves as the injection current increases. In the initial measurements, there appears to be only a single peak, but a second peak at a smaller wavelength begins to grow. Their published results are reproduced in Figure 4.7.

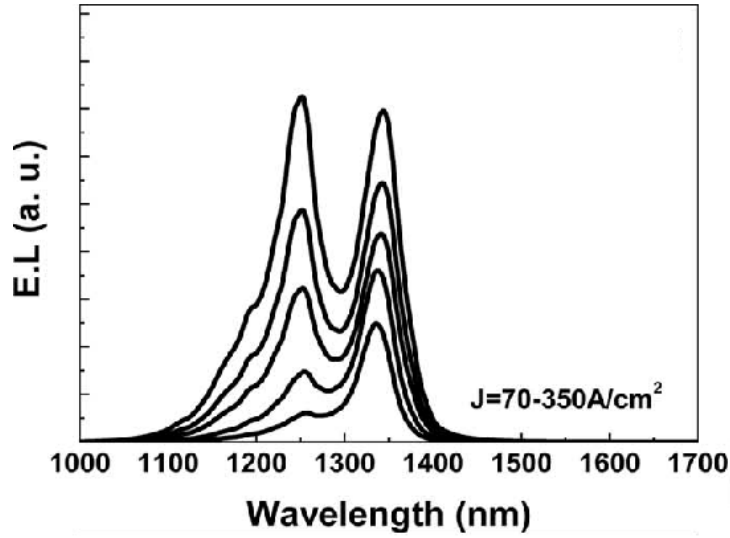


Figure 4.7 Optical power spectra for a passively mode-locked InAs/GaAs QD laser using injection current densities ranging from 70-350 A/cm², from published results [20]

Though some slight adjustments need to be made to translate the injection current densities described in the paper into injection current values, these results can easily be recreated using the perturbation theory model to show how it can demonstrate lasing from multiple wavelengths. All of the relevant values are inferred from the publication, and are reproduced in Table 4.3.

Table 4.3 List of specific parameters used to simulate results published by Majid *et al.* [20]

Name	Expression	Value	Description
nb	3.34	3.34	Effective Refractive Index
Nqw	5	5	Number of QW Layers
Nd	$2.7 \times 10^{10} [1/\text{cm}^2]$	$2.7 \times 10^{14} 1/\text{m}^2$	QD Surface Density
Dip	$0.72 [\text{eV} \cdot \text{nm}]$	$1.1536 \times 10^{-28} \text{ kg} \cdot \text{m}^3/\text{s}^2$	Dipole Matrix Element
T	293[K]	293 K	Temperature
L	8.7[mm]	$8.7 \times 10^{-3} \text{ m}$	Cavity Length
W	7[um]	$7 \times 10^{-6} \text{ m}$	Ridge Width
H	10[nm]	$1 \times 10^{-8} \text{ m}$	QD Layer Height
lam0	1550[nm]	$1.550 \times 10^{-6} \text{ m}$	Central Lasing Frequency
J	70[A/cm ²], 140[A/cm ²], 210[A/cm ²], 280[A/cm ²], 350[A/cm ²]	$7 \times 10^5 \text{ A/m}^2$, $1.4 \times 10^6 \text{ A/m}^2$, $2.1 \times 10^6 \text{ A/m}^2$, $2.8 \times 10^6 \text{ A/m}^2$, $3.5 \times 10^6 \text{ A/m}^2$	Laser Injection Current Density

After all of these publications were studied and all relevant information was entered into the perturbation theory simulation, several large data sets were generated so that we can analyze the results and see how well they compare to the actual published results. These simulated results are reproduced in Figure 4.8.

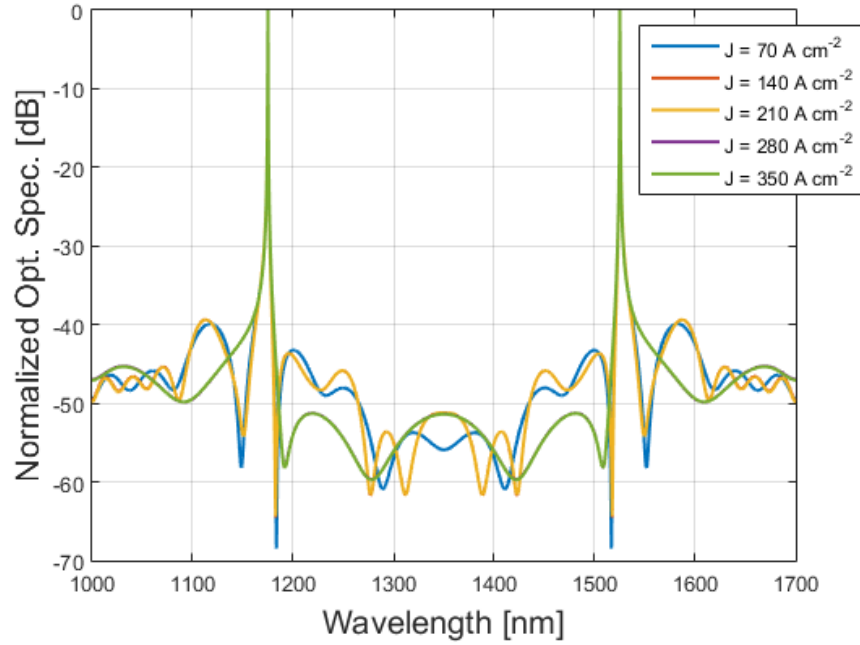


Figure 4.8 Optical power spectra for a passively mode-locked InAs/GaAs QD laser using injection current densities ranging from 70-350 A/cm², from perturbation theory simulation

Chapter 5 – Investigation

5.1 Introduction

A detailed analysis of the simulation results presented in Chapter 4, as well as how accurately it can replicate published results, will be presented. The simulated results showing agreement with the experimental data will confirm the validity of some of the assumptions that were made when designing the model.

First, the generated RF spectra will be examined in more detail, along with how it compared the published results, both theoretical and experimental. This is coupled with an analysis of what is seen in the published results, as well as possible explanations for the behaviour shown in the simulation. The RF spectrum is very important for identifying the presence of mode-locking, as it is expected to see a reduction in the line-width as the frequency difference between modes becomes constant. [14]

Next, focus is put on the results for the time domain behaviour of the electric field. This is the primary focus of our study on mode-locking, so it is of particular attention. The details of the pulsing behaviour seen in the experimental results is discussed, and the perturbation theory simulation results are compared to them. An analysis of the behaviour seen from the simulation and how it compares to the experimental data is presented.

Finally, the power spectra produced by the laser, both experimentally and in the perturbation theory simulation, is studied. Of particular interest is the causes of both broadening of peaks in the spectrum as well as the presence of lasing peaks from two distinct wavelengths.

5.2 RF Spectra

Figure 4.1 presents a comparison between the RF spectra generated by the TDTW model explored by Bardella *et al.* [15][16] and the ones generated using the perturbation theory model. When we then look at the power spectra generated by the perturbation theory simulation, we can see the expected lasing as indicated by the positive gain around the central frequency. We also see that the lasing peak is much broader at the lower injection current, whereas the higher injection current leads to a narrower peak, just as in the published results from the TDTW simulation.

As discussed earlier, inhomogeneous gain broadening in the spectrum is caused by the variation of the sizes of the QDs. [9] Since the optical properties of QDs are heavily influenced by physical characteristics like size, and limits in fabrication techniques make it difficult to limit size variation in the dots, QD lasers will often emit light along a wider range of wavelengths than the idealized picture. Unfortunately, the perturbation theory simulation is unable to properly exhibit broadening to the extent that is expected. Though it uses a density of state functions which include some degree of broadening, this is only accomplished through an arbitrary coefficient. In reality, the broadening is caused by the varying distribution of dot sizes, something lacking within this model as only a single dot was used.

Additionally, the perturbation theory simulation does not show significant differences in terms of the relative intensities of the peaks. In contrast, in the published results from the TDTW simulation, we see a very large peak at the central frequency above the lasing threshold, but below the threshold the peak is much smaller. The perturbation theory model still has a noticeable peak at the central frequency in both cases, indicating the presence of lasing, but the differences in their maximum intensities isn't as prominent.

Though the activity here has no significant connection to mode-locking or the role of four-wave mixing, these results do illustrate that the perturbation theory model for QD lasers is able to demonstrate lasing activity in the appropriate circumstances, but cannot properly illustrate the effects of inhomogeneous gain broadening.

Now, when looking at the perturbation theory simulation's results in Figure 4.4, we can see very similar behaviour to what was seen in Figure 4.3. Once again we see a very prominent peak at the central frequency when above the lasing frequency, so once again the simulation is able to properly show lasing behaviour. The difference in the amount of broadening seen below and above the current threshold is not as apparent as in the previous data sets, but this detail is also not present in the experimental results in this case.

Another important feature within the experimental data is that we start to see a peak emerge at a second wavelength separate from the central wavelength. Though it is not a very high power peak, it is still evident. This feature is not seen in the data from the perturbation theory simulation, which attempts to recreate such behaviour through the presence of multiple modes in

the cavity. Though it is set up so that we can use as many modes as we like, adding more nodes to the simulation also leads to a large increase in the amount of memory needed to solve all of the equations, making it very computationally expensive. In this case, only 3 modes were used, so it is likely this effect isn't very prominent due to the limited number of modes. The cavity being simulated is very large ($\sim 10^{-6}$), which requires a large amount of memory, further limiting the number of modes we can reasonably use when calculating the spectrum.

Similar to the inhomogeneous gain broadening, which is not properly incorporated due to the model simulating only a single dot, this element is limited by the currently simplified state of the perturbation theory simulation. With a more efficient algorithm or more computational resources, it may be possible to use both a larger number of modes and a larger number of dots, and therefore show more broadening and lasing from multiple wavelengths.

5.3 Time Domain Pulses

When studying the time domain electric field behaviour of the device studied by Tierno *et al.* [19], periodically repeating time-domain electric field behaviour is evident both in the experimental data and in the data generated by the perturbation theory simulation, as represented in Figure 4.6. However, the simulation results differ somewhat from what is seen in the experimental data. First of all, though periodic behaviour is very evident in the varying electric field, it is very obviously sinusoidal in contrast to the pulses seen in the experimental data. The period of the sinusoidal simulated field also has a much faster repetition rate than reported, with the gain cycle repeating so frequently that the individual wave-forms cannot be clearly seen on larger time scales. By looking at smaller 100 ns segments of the full time domain of each data set in Figure 5.1, the period and how it varies can be more clearly discerned.

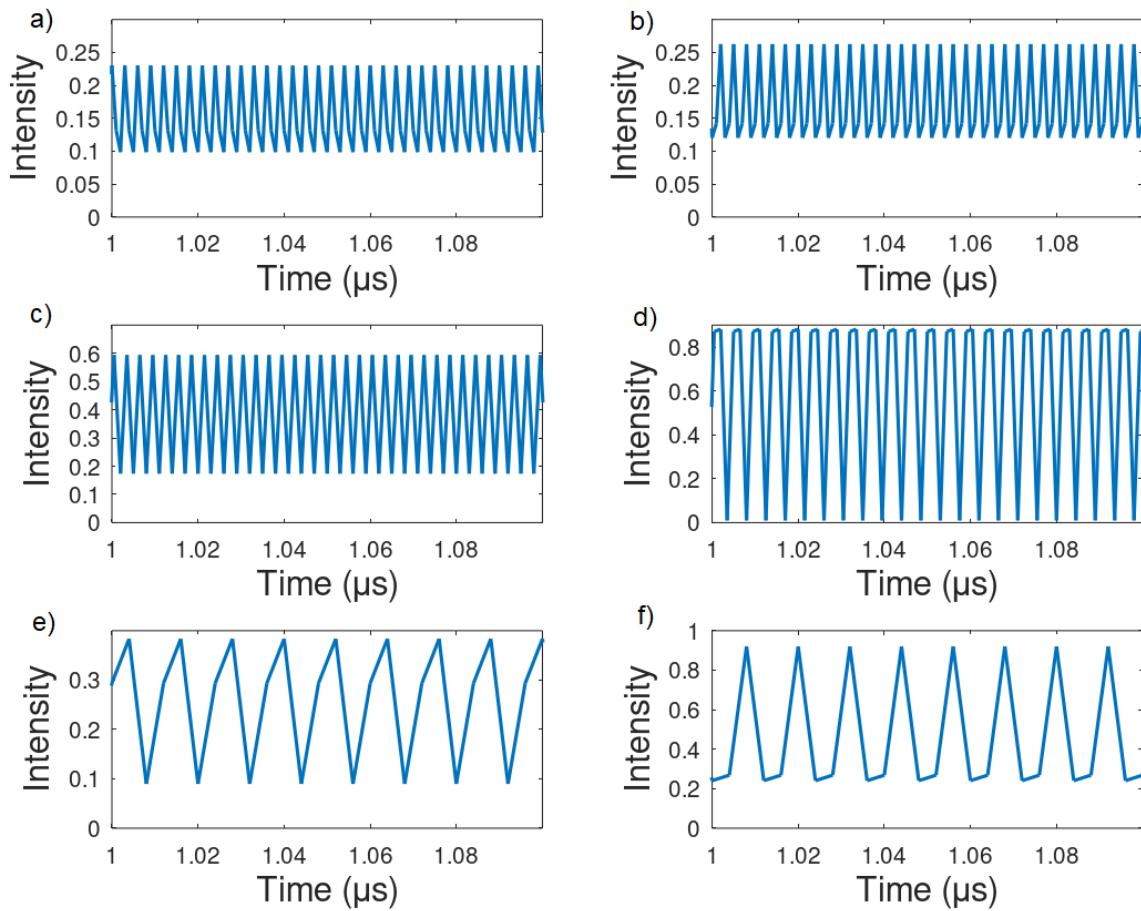


Figure 5.1 Small segments of the time domain electric field behaviour of a 3.5 mm InAs QD laser with an injection current of a) 803 mA, b) 827 mA, c) 832 mA, d) 840 mA, e) 872 mA, and e) 910 mA

Though the exact period may differ somewhat from the period seen in experimental results, we can see in both sets of data that the period varies as the injection current increases. However, the trend is not the same. In the experimental data, we see the period shorten as we increase the injection current from 803 mA to 827 mA (5 peaks in 1.5 μm becomes 7 peaks in 1.5 μm), while with the simulated results the period increases, as we see 27 peaks in 40 ns at 803 mA and only 13 peaks at 827 mA. As the injection currents get higher, the experimental results show the period consistently decreasing, whereas the simulation results show the period increasing as

we increase the current, with the one exception being a small decrease in period as the current goes from 827 mA (33 peaks in 100 ns) to 832 mA (34 peaks in 100 ns).

Despite these drawbacks, periodic time domain behaviour is evident in the electric field data. Though the same kinds of pulses seen experimentally are not present in the simulated data, which instead appear more sinusoidal, the electric field intensity still varies significantly with time, to extent that this cannot be said to be a continuously operating laser. Additionally, there is a very consistent period in the variations from high intensity to low intensity within individual sets of data. Although the exact period differs from what has been published, the same trend of the period varying as the injection current is changed is still apparent.

The more sinusoidal character of the electric field suggests some deeper issues with the simulation's treatment of mode-locking. In addition to the issues related to the timing of the gain cycle, the lack of distinct pulses suggest a lack of mode-locking despite there still being clear periodic behaviour. In order for the effects of the modes being locked to be evident there needs to be a large number of modes interacting with each other, which is not happening due to the simulation's limited treatment of inhomogeneous gain broadening and the small number of modes used.

When compared to the TDTW simulation, the most prominent difference is how the interactions between carriers and light are treated. Whereas the TDTW model treats the basic dynamics of the system, this model looks at individual interactions between electrons and electromagnetic waves through the application of quantum perturbation theory, and how these waves interfere with each other to produce four wave mixing. [17] These changes have a large impact on both the equations for the carrier populations and the electric field, and are intended to influence the pulsing behaviour caused by mode-locking in the laser cavity. As far as the general lasing behaviour goes, including spectral broadening and lasing from multiple wavelengths, the perturbation theory model performs as well as the TDTW model, but struggles with presenting inhomogeneous gain broadening and the formation of pulses. Despite these discrepancies, high frequency repetitive peaks are evident within the perturbation theory simulation where they could not be produced with the TDTW model.

Looking into the equations in the perturbation theory model, the primary driver of the pulsing behaviour in the rate equation for the generalized 3rd-order coefficient (eq. 2.43), which mostly depends on the band structure, but is also heavily dependent on the population inversion. This contribution of the population inversion is how the carrier population rate equations become involved in the system. In this case, results reproduced in Figure 5.2 clearly indicate the presence of a population inversion among the carriers in the system. The highest energy levels, N_4 and N_5 , are much more highly populated than all of the lower energy levels. However, it is important to note that this state isn't completely static.

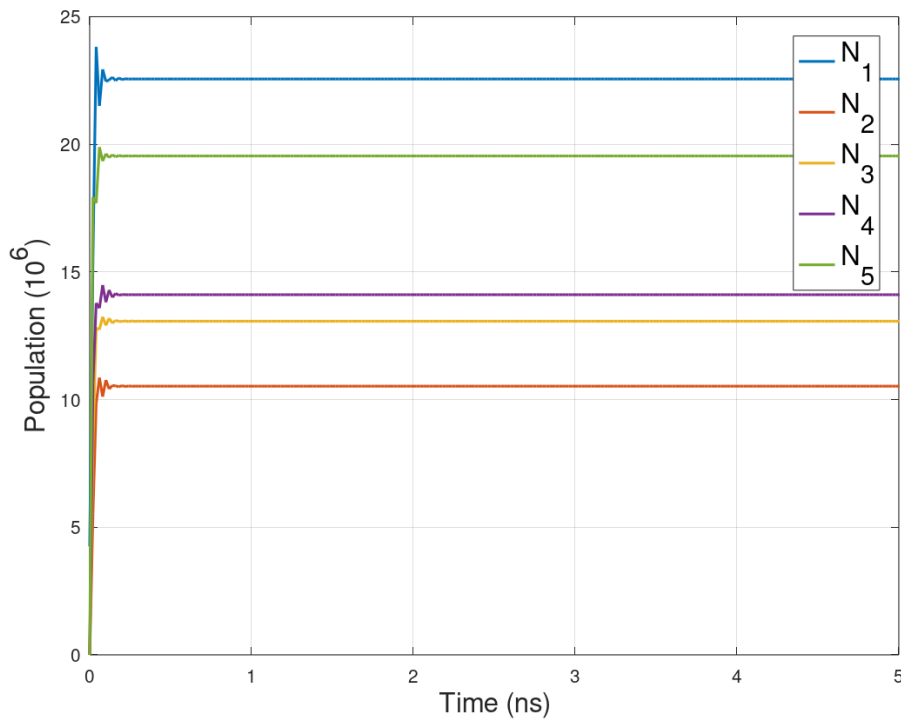


Figure 5.2 Simulated carrier dynamics of a 3.5 nm InAs QD with an injection current of 803 mA

Though from the figure we can see that the overall relative populations very quickly relax to a constant state, individual carrier transitions are still occurring between different energy levels, and as seen in eq. 2.56-2.60, these transitions depend on the lifetimes of each individual level. As such, the lifetimes can be seen as an important driver of the time domain behaviour of

the system. In addition to the other issues described, the discrepancies in the exact timing may be a consequence of the lifetime values that were used. These values were estimated based off of the properties of the materials used, but a more detailed study may be required for a more detailed treatment of this facet of the model.

5.4 Optical Spectrum

Finally, looking at the optical spectrum data will give us another opportunity to assess the ability of the simulation to show lasing from two distinct wavelengths. In both Figure 4.7 (experimental) and 4.8 (simulation), we can clearly see lasing from two separate peaks. Unlike in Figure 4.4, we can clearly see lasing from the second peak in the data generated by the perturbation theory model, so although this run of the simulation did not use a larger number of cavity modes, the separate peaks are still apparent.

Though the perturbation theory model is able to properly show the general broadening behaviour we expect in this case, there are still some issues which keep it from closely matching the experimental data. One of the most notable traits of the published experimental results is that the relative intensity of the two peaks changes as the injection current varies. Initially, the peak around 1350 nm dominates, but as the injection current increases the peak at 1225 nm becomes larger and larger until they are at approximately equal magnitude. When the same data is generated using the simulation, the two peaks are the same size at all tested injection currents.

The authors of the paper attribute this characteristic seen in their published results to the specific structure of their QD layers and the details of the fabrication. The device they are studying features closely stacked layers of InAs and GaAs QDs, with an InGaAs cap. [20] As discussed earlier, the current state of the simulation is that it is only simulating a single QD rather than hundreds. As such, this level of detail cannot be properly incorporated into the current version of the simulation. Although it was possible to incorporate important experimentally derived parameters for InGaAs QDs, [26] detailed information on the specific band structure of the active medium would require a more specialized treatment of the geometry and structure of the device.

The presence of lasing from two separate wavelengths is the result of emissions from two different transitions between bands in the active medium, so an accurate view of the band structure of the results is required to accurately replicate this effect. The perturbation theory simulation's model is able to properly show lasing from two different wavelengths, but a more accurate treatment of the band structure of the dots would be able to more accurately portray the way the relative intensities vary as the injection current increases.

Despite the general trend of lasing from two different wavelengths being present, when we look into the more specific details the simulated spectrum does not match very closely with the published results. Notably, the peaks are much more narrow, and the spectrum is overall much noisier than what was seen experimentally. The specific wavelengths where the lasing is occurring is also different, with the peaks in the experimental data occur around 1225 μm and 1350 μm , whereas the simulated peaks occur at 1175 μm and 1525 μm . The first peaks are occurring at similar wavelengths, but the second are occurring at very different wavelengths, off by nearly 200 μm . The narrowing of the peaks compared to the experimental data may be a result of not using enough modes in the simulation, but their positioning in the spectra are a different matter. Since the specific energy of the emissions and thus the wavelengths where the lasing occurs depends on the change in energy which occurs with each transition, the previous alluded to inaccuracies in the representation of the device's band structure could contribute to the large discrepancy seen in the second lasing wavelength.

Though this element requires some improvement, on a fundamental level many of expected behaviours can be seen. The theoretical model used was able to show the lasing from two separate wavelengths when expected, and looking at the time-domain electric field measurements reproduced in Figure 5.3 shows the same periodic time-domain behaviour which was observed earlier, including the switching on behaviour.

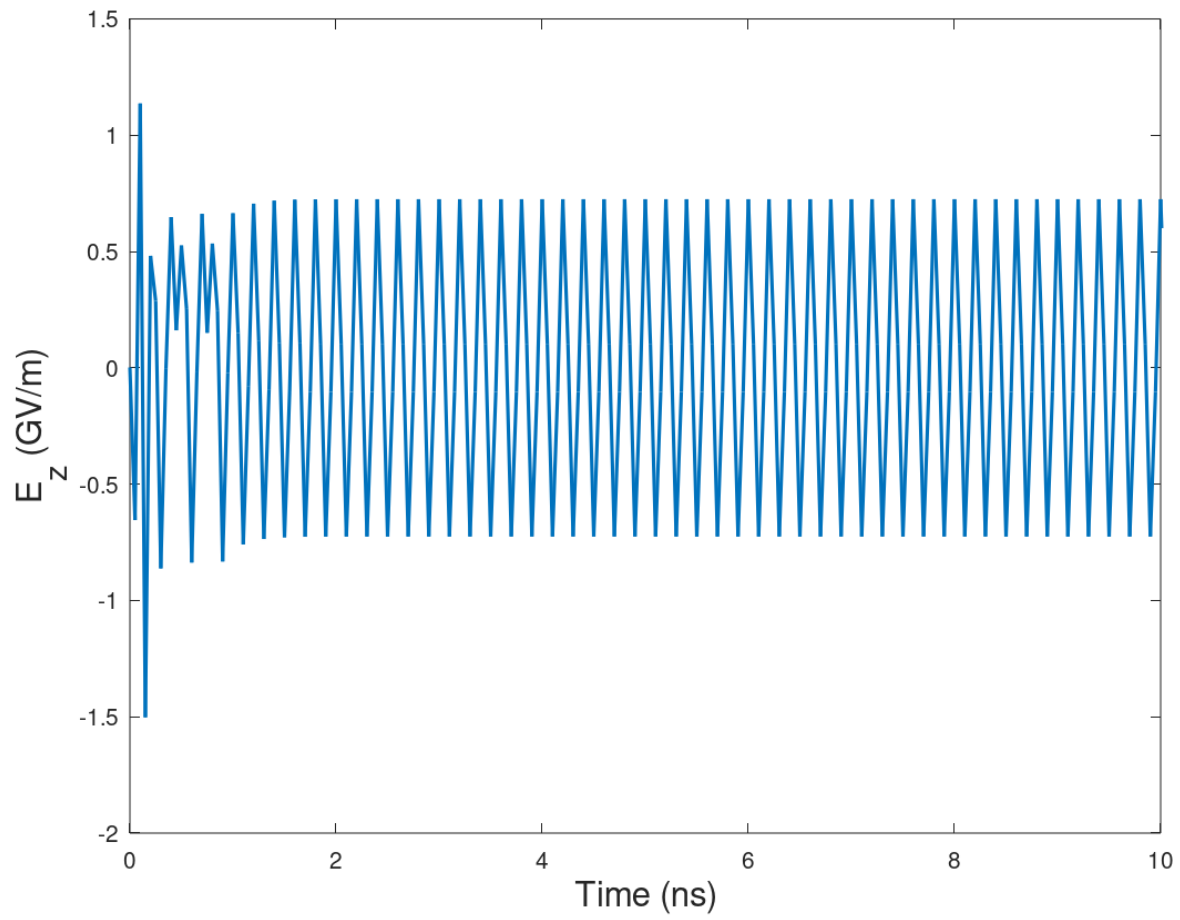


Figure 5.3 Time domain electric field behaviour of a InAs/GaAs QD with an injection current density of 70 A/cm^2 as modelled using the perturbation theory simulation

Chapter 6 – Conclusion

Though there are flaws in the results obtained using the current version of the perturbation model, much of the general lasing behaviour and other key characteristics of the data matches the expected trends to the same degree as the TDTW mode. Though the perturbation theory simulation's main weaknesses were the lack of inhomogeneous gain broadening and cavity modes, these issues arise from its limited treatment of the device geometry, which only simulates a single dot.

When attempting to illustrate these important characteristics by replicating the findings of previous simulations of mode-locked QD lasers, there was close agreement with much of the general lasing behaviour despite some difficulties with mode-locking. The frequency domain RF spectra which were generated all show lasing at the expected frequencies, though they show some differences from both the results of a TDTW simulation and some experimental data. There was a smaller degree of inhomogeneous gain broadening in the perturbation theory simulation, which is likely related to the current iteration of the simulation only simulating a single dot. These issues can be resolved with a more detailed treatment of the device geometry, leading to more broadening in the spectra, or an alternative approach to the distribution of dot sizes like what is used in the TDTW model. Though there are still flaws with the current iteration of the perturbation theory simulation, it still matches the TDTW simulations fairly well and the ways to improve it are well understood.

Experimental data from an InAs-based QD laser was replicated with some accuracy by the perturbation theory model. The simulation was able to replicate the periodic behaviour similar to that seen in the recorded experimental data, but the period of the gain cycle didn't quite match with the experimental data. The behaviour was also very sinusoidal, in contrast to the distinctive pulsing behaviour seen experimentally. Although the timing wasn't exactly the same, the general trend of the period varying as the injection current was raised was still evident. The accuracy of this overall behaviour shows that the new theoretical model and its implementation reflects some of the dynamics of such a system, as the discrepancies in the specific timing may suggest issues with the specific values chosen rather than the methodology. The repetition rate of the gain cycle depends very strongly on the lifetimes of each energy level, so these issues are tied to

insufficiently accurate values picked for these parameters. The fact that the timing used here also appears to be much faster could also contribute to the lack of distinct pulses like we see in the experimental data. Though these general behaviours are still evident, the model will need to be expanded to include more cavity modes and more QDs to ensure the presence of interactions between different modes leading to the mode-locking and the distinct pulses observed in the experimental data. Similarly, new modules could be added to separately calculate more accurate values for the relevant lifetimes.

The perturbation theory model was also used to reproduce data from an InAs/GaAs QD laser showing lasing from two distinct wavelengths. The time domain behaviour of the carrier populations produced with the perturbation theory simulation still showed the same stable population inversion, and also showed lasing from two distinct peaks. However, the behaviour of the two peaks in the power spectra didn't perfectly match, as the experimental data showed the changing relative intensity of the two peaks as the injection current density increased. The two peaks in the simulated spectra also did not closely line up with the experimental data, with the second peak being at a noticeably longer wavelength and both peaks being much sharper. This effect of lasing from two distinct wavelengths arises due to two dominant transitions of different energies, which can arise due to the band structure of the device. The structure used in this simulation was that of a single dot, and therefore it lacked many of the unique characteristics of the device used in the published results. Though either more accurate values or a method of calculating a device's band structure could be incorporated into the simulation for improved results, the inaccuracies don't appear to be fundamental to the model. The narrowness of the peaks may also be related to computational limitations restricting the number of lasing modes which can be used in the current simulation.

Though there are no published simulation results for this data which the perturbation theory simulation can be compared to, a replication of the model explored by Bardella *et al.* [19] was used to replicate these results to see how the outcomes compare to the perturbation theory model. However, though such results have not been published previously, a replication of their model was used alongside the perturbation theory model. This simulation is reproduced within the Appendix. Though this recreation of the Bardella *et al.* simulation was effective for smaller

devices, it is much more mathematically complex and therefore much more memory intensive, and thus is unable to properly simulate lasing activity in the larger cavities studied by Tierno *et al.* and Majid *et al.* Thus, a direct comparison with the TDTW model is not possible, but the fact that these results can only be obtained using the perturbation theory simulation shows that it is more useful.

The effectiveness of the perturbation theory model in exhibiting the general trends of the properties of these devices, especially in comparison with previously attempts, shows the validity of some of the assumptions that went into this model. However, despite many of these advantages, there are some changes that will need to be made to the model moving forward. In addition to minor issues caused by inaccurately selected parameters, particularly lifetimes and band structure, the simulation is largely held back by its limited treatment of inhomogeneous gain broadening. This issue limits its ability to properly simulate mode-locking, as well as lasing from multiple wavelengths, and is largely caused by the device geometry consisting of only a single dot. These issues can be resolved by either treating inhomogeneous gain broadening in a manner similar to the TDTW model, or by using more detailed treatments of the device's geometry to show several QDs with different sizes. Thankfully, due to COMSOL's modular design, it should be possible to add on further modules which can more accurately represent these characteristics of the devices, as well as more accurately derive values that were previously estimated based on the literature. However, these elements, as well as the use of more cavity modes, will be very computationally expensive.

Although the perturbation theory model presented here has some drawbacks in its current form, the cause of these weaknesses are clear based on how it performs compared to the TDTW model and published experimental results. With these causes well understood, these findings present clear steps which can be taken to improve the model to a state where it may have some predictive power. Such a model can also be used to help plan further research and assess which device properties may be desirable before fabrication. In this case, further work and refinement on the simulation, as outlined in this section, has the potential to bear much fruit.

References

- [1] S. Kasap, and P. Capper, *Springer handbook of electronic and photonic materials*, Springer, 2006
- [2] Yudhistira, F. Rahayu, and Y. Darma, "Simulation of spontaneous emission power on silicon based quantum dot with variation of light source and dot size," *2011 2nd International Conference on Instrumentation, Communications, Information Technology, and Biomedical Engineering*, 2011
- [3] T. W. Schlereth, S. Gerhard, W. Kaiser, S. Hofling, and A. Forchel, "High-performance Short-Wavelength (~760 nm) AlGaInAs Quantum-Dot Lasers," *IEEE Photonics Technology Letters*, vol. 19, pp. 1380-1382, 2007
- [4] V. J. Wittwer, C. A. Zaugg, W. P. Pallmann, A. E. H. Oehler, B. Rudin, M. Hoffmann, M. Golling, Y. Barbarin, T. Südmeyer, and U. Keller, "Free-running quantum dot SESAM modelocked VECSEL with record-low timing jitter," *2011 Conference on Lasers and Electro-Optics Europe and 12th European Quantum Electronics Conference*, 2011
- [5] W. W. Chow, H. C. Schneider, E. J. Pearce, and P. M. Smowton, "Absence of filamentation in quantum dot lasers. Theory and experiment," *IEEE 18th International Semiconductor Laser Conference*, 2002
- [6] N. Kirkstaedter, N. N. Ledentsov, M. Grundmann, D. Bimberg, V. M. Ustinov, S. S. Ruvimov, M. V. Maximov, P. S. Kop'ev, Z. I. Alferov, U. Richter, P. Werner, U. Gosele, and J. Heydenreich, "Low threshold, large T injection laser emission from InGaAs quantum dots," *Electron. Lett.*, vol. 30, pp. 1416-1417, 1994
- [7] N. N. Ledentsov, V. M. Ustinov, A. Y. Egorov, A. E. Zhukov, M. V. Maksimov, I. G. Tabatadze, and P. S. Kop'ev, "Optical properties of heterostructures with InGaAs-GaAs quantum clusters," *Semiconductors*, vol. 28, pp. 832-834, 1994
- [8] H. A. Haus, "Mode-Locking of Lasers," *IEEE Journal on Selected Topics in Quantum Electronics*, vol. 6, no. 6, pp. 1173-1185, 2000

- [9] E. Rafailov, M. Cataluna, and W. Sibbett, "Mode-locked quantum-dot lasers," *Nature Photon.*, vol. 1, pp. 395-401, 2007
- [10] A. Gubenko, D. Livshits, I. Krestnikov, S. Mikhrin, A. Kozhukov, A. Kovsh, N. Ledentsov, A. Zhukov, and E. Portnoi, "High-power monolithic passively modelocked quantum-dot laser," *Electronics Letters*, vol. 41, no. 20, pp. 1124-1125, 2005
- [11] N. Kirkstaedter, N. N. Ledentsov, M. Grundmann, D. Bimberg, V. M. Ustinov, S. S. Ruvimov, M. V. Maximov, P. S. Kop'ev, Zh. I Alferov, U. Richter, P. Werner, U. Gösele, and J. Heydenreich, "Low threshold, large T_0 injection laser emission from (InGa)As quantum dots," *Electronics Letters*, vol. 30, no. 17, pp. 1416-1417, 1994
- [12] J. K. Mee, M. T. Crowley, N. Patel, D. Murrell, R. Raghunathan, A. Aboketaf, A. Elshaari, S. F. Preble, P. Ampadu, and L. F. Lester, "A passively mode-locked quantum-dot laser operating over a broad temperature range," *Appl. Phys. Lett.*, vol. 101, no. 7, 2012
- [13] Z. Jiao, R. Zhang, X. Zhang, J. Liu, and Z. Lu, "Modeling of Single-Section Quantum Dot Mode-Locked Lasers: Impact of Group Velocity Dispersion and Self Phase Modulation," *IEEE Journal of Quantum Electronics*, vol. 49, no. 12, pp. 1008-1015, 2013
- [14] P. Bardella, C. Weber, L. L. Columbo, L. F. Lester, M. Gioannini, and S. Breuer, "RF line width and integrated RIN study of a single-section quantum dot comb laser," *Proc. Of SPIE*, vol. 10682, no. 1068223, 2018
- [15] M. Rossetti, P. Bardella, and I. Montrosset, "Time-Domain Travelling-Wave Model for Quantum Dot Passively Mode-Locked Lasers," *IEEE Journal of Quantum Electronics*, vol. 47, no. 2, pp. 139-150, 2011
- [16] P. Bardella, L. L. Columbo, M. Gioannini, "Self-generation of optical frequency comb in single section Quantum Dot Fabry-Perot lasers: a theoretical study," *Optics Express*, vol. 25, no. 12, 2017
- [17] W. W. Chow, S. Liu, Z. Zhang, J. E. Bowers, and M. Sargent III, "Multimode description of self-mode locking in a single section quantum-dot laser," *Optics Express*, vol. 28, no. 14, 2020

- [18] W. W. Chow and S. W. Koch, "Theory of Semiconductor Quantum-Dot Laser Dynamics," *IEEE Journal of Quantum Electronics*, vol. 41, no. 4, 2005
- [19] A. Tierno, N. Radwell, and T. Ackerman, "Low-frequency self-pulsing in single section quantum-dot laser diodes and its relation to optothermal pulsations," *Physical Review A*, **84**, 043828, 2011
- [20] M. A. Majid, D. T. D. Childs, H. Shahid, S. Chen, K. Kennedy, R. J. Airey, R. A. Hogg, E. Clarke, P. Howe, P. D. Spencer, and R. Murray, "Toward 1550-nm GaAs-Based Lasers Using InAs/GaAs Quantum Dot Bilayers," *IEEE Journal of Selected Topics in Quantum Electronics*, vol. 17, no. 5, 2011
- [21] A. Gordon, C. Y. Wang, L. Diehl, F. X. Kärtner, A. Belyanin, D. Bour, S. Corzine, G. Hofler, H. C. Liu, H. Schneider, T. Maier, M. Troccoli, J. Faist, and F. Capasso, "Multimode regimes in quantum cascade lasers: From coherent instabilities to spatial hole burning," *Physical Review A*, vol. 77, no. 5, 2008
- [22] Z. G. Lu, J. R. Liu, S. Raymond, P. J. Poole, P. J. Barrios, and D. Poitras, "312-fs pulse generation from a passive C-band InAs/InP quantum dot mode-locked laser," *Optics Express*, vol. 16, no. 14, pp. 10835-10840, 2008
- [23] E. G. Barbagiovanni, D. J. Lockwood, P. J. Simpson, L. V. Goncharova, "Quantum confinement in Si and Ge nanostructures: Theory and experiment," *Applied Physics Reviews*, vol. 1, no. 1, 2014
- [24] C. Burda, X. Chen, R. Narayanan, M. A. El-Sayed, "Chemistry and Properties of Nanocrystals of Different Shapes," *Chemical Reviews*, no. 125, pp. 1025-1102, 2005
- [25] S. Singh, M. Festin, W. R. T. Barden, L. Xi, J. T. Francis, and P. Kruse, "Universal Method for the Fabrication of Detachable Ultrathin Films of Several Transition Metal Oxides," *ACS Nano*, vol. 2, no. 11, 2008
- [26] E. Rajaei, and M. A. Borji, "Energy Levels of InGaAs/GaAs Quantum Dot Lasers with Different Sizes," *International Journal of Nanoscience and Nanotechnology*, vol. 12, no. 1, pp. 45-53, 2016

- [27] D. Chithrani, R. L. Williams, J. Lefebvre, P. J. Poole, G. C. Aers, "Optical spectroscopy of single InAs/InP quantum dots around $\lambda=1.55 \mu\text{m}$," *Physica E*, vol. 21, pp. 290-294, 2004
- [28] C. Ratsch, and A. Zangwill, "Equilibrium theory of the Stranski-Krastanov epitaxial morphology," *Surface Science*,
- [29] Z. Lu, J. Liu, S. Raymond, P. Poole, P. Barrios, G. Pakulski, D. Poitras, F. Sun, S. Taebi, and T. Hall, "Ultra-broadband quantum-dot semiconductor optical amplifier and its applications," in *Optical Fiber Communication Conference and the National Fiber Optic Engineers Conference*, 2007
- [30] K. Mukai, N. Ohtsuka, H. Shoji, and M. Sugawara, "Phonon bottleneck in self-formed $\text{In}_x\text{Ga}_{1-x}\text{As}/\text{GaAs}$ quantum dots by electroluminescence and time-resolved photoluminescence," *Physical Review B*, vol. 54, pp. R5243-R5246, 1996
- [31] E. U. Rafailov, S. J. Whit, A. A. Lagatsky, A. Miller, W. Sibbett, D. A. Livshits, A. E. Zhukov, and V. M. Ustinov, "Fast quantum-dot saturable absorber for passive mode-locking of solid state lasers," *IEEE Photonics Technology Letters*, vol. 16, pp. 2439-2441, 2004
- [32] P. Borri, W. Langbein, J. M. Hvam, F. Heinrichsdorff, M. H. Mao, and D. Bimberg, "Ultrafast gain dynamics in InAs-InGaAs quantum dot amplifiers," *IEEE Photonics Technology Letters*, vol. 12, no. 6, pp. 594-596
- [33] P. Borri, W. Langbein, J. M. Hvam, F. Heinrichsdorff, M. H. Mao, and D. Bimberg, "Spectral hole-burning and carrier-heating dynamics in InGaAs quantum-dot amplifiers," *IEEE Journal of Selected Topics in Quantum Electronics*, vol. 6, no. 3, pp. 544-551, 2000
- [34] L. Coldren and S. Corzine, *Diode lasers and photonic integrated circuits*, Wiley, 1995
- [35] M. Gioannini, and I. Montrosset, "Numerical analysis of the frequency chirp in quantum-dot semiconductor lasers," *IEEE Journal of Quantum Electronics*, vol. 43, pp. 941-949, 2007
- [36] M. Sargent III, M. O. Scully, and W. E. Lamb Jr, *Laser Physics*, Addison-Wesley, 1974

- [37] W. W. Chow, S. W. Koch, and M. Sargent III, *Semiconductor-Laser Physics*, Springer-Verlag, Heidelberg, 1994
- [38] H. Risken and K. Nummedal, “Self-pulsing in lasers,” *Journal of Applied Physics*, vol. 39, no. 10, 2003
- [39] R. Graham, and H. Haken, “Quantum theory of light propagation in a fluctuating laser-active,” *Zeitschrift für Physik A Hadrons and nuclei*, 1968
- [40] A. Franceschetti, and A. Zunger, “Pseudopotential calculations of electron and hole addition spectra of InAs, InP, and Si quantum dots,” *Physical Review B*, vol. 62, no. 4, 2000

Appendix

Full code of the COMSOL simulation for the Bardella *et al.* data, converted into MATLAB

MATLAB code used to analyze the raw data using the electric field values

```
close all;
format long e;
pkg load signal;

ita_i=1; %imaginary unit
epsilon0=8.85e-12; %permittivity in vacuum
c=3e8; %speed of light (vacuum)
e=1.602e-19; %electron charge
m0=9.1095e-31; %electron rest mass
kB=1.3806e-23; %Boltzmann (J/K)
h=6.63e-34; %Planck (Js)
hbar=h/2/pi; %reduced Planck

lambda0=1.560-6;
omega0=c/(lambda0/2/pi);

t1=round(length(Eout)/10);
t2=length(Eout);
dt=time(3)-time(2);
E=Eout(t1:t2);
df=1/(t2-t1+1)/dt;
fmax=1/dt/2;
fFFT=round(-fmax:df:fmax-df);
f0=omega0/2/pi;
lambdaFFT=c./(fFFT+f0);
x=t2-t1;
F=(abs(fftshift(fft(E))))).^2/x^2;
F_dBm=10*log10(F/mean(F));
Fmax_dBm=max(F_dBm);
norm_spectrum=F_dBm-Fmax_dBm;
compat=pwelch('psd');
[pxx,f]=pwelch(E/mean(E),length(fFFT));
pwelch(compat);
f_m=linspace(f(1),f(length(f)),length(F_dBm));
P=E.*conj(E)/1e-3;
Pavg=mean(P);

omega=linspace(2*pi*220e12,2*pi*280e12,20000);
lambda=c./(omega/2/pi);
```

```

figure(1);
plot(time/1e-12,Eout.*conj(Eout)/1e-3);xlim([0,time(t2)/1e-12]);
ylim([min(Eout.*conj(Eout)/1e-3),max(Eout.*conj(Eout)/1e-3)]);
xlabel('Time (ps)');ylabel('Intensity (mW)');

figure(2);
plot(time(t1:t2)/1e-12,P);xlim([time(t1)/1e-12,time(t2)/1e-12]);
ylim([min(P),max(P)]);xlabel('Time (ps)');ylabel('Intensity
(mW)');

figure(3);
plot(lambdaFFT/1e-9,F_dBm);grid;xlabel('Wavelength [nm]');
xlim([(lambda0/1e-9)-30,(lambda0/1e-9)+30]);ylabel('Optical
Spectrum [dBm]');

figure(4);
plot(lambdaFFT/1e-9,F_dBm);grid;xlabel('Wavelength [nm]');
xlim([(lambda0/1e-9)-20,(lambda0/1e-9)+20]);ylabel('Optical
Spectrum [dBm]');

figure(5);
plot(lambdaFFT/1e-9,F_dBm);grid;xlabel('Wavelength [nm]');
xlim([(lambda0/1e-9)-10,(lambda0/1e-9)+10]);ylabel('Optical
Spectrum [dBm]');

figure(6);
plot(lambdaFFT/1e-9,norm_spectrum);grid;xlabel('Wavelength
[nm]');
ylabel('Normalized Opt. Spec. [dB]');

figure(7);
plot(f,10*log10(pxx));grid;xlabel('Frequency [Hz]');ylabel('Opt.
Spec. [dB]');

figure(8);
plot(f_m,F_dBm);grid;xlabel('Frequency [Hz]');ylabel('Opt. Spec.
[dB]');

figure(9);
plot(c./(lambdaFFT/1e-9),norm_spectrum);grid;xlabel('Frequency
[Hz]');
ylabel('Opt. Spec. [dB]');

```

MATLAB code used to analyze the raw data using the population values

```
close all;
format long e;
pkg load signal;

%%Constants%%%%%%%%%%%%%%%%%%%%%%%%%%%%%%%%%%%%%%%%%%%%%%%%%%%%%%%%%%
%%%%%%%%%%%%%%%%%%%%%%%%%%%%%%%%%%%%%%%%%%%%%%%%%%%%%%%%%%
ita_i=1; %imaginary unit
epsilon0=8.85e-12; %permittivity in vacuum
c=3e8; %speed of light (vacuum)
e=1.602e-19; %electron charge
m0=9.1095e-31; %electron rest mass
kB=1.3806e-23; %Boltzmann (J/K)
h=6.63e-34; %Planck (Js)
hbar=h/2/pi; %reduced Planck

%%Main Model Parameters%%%%%%%%%%%%%%%%%%%%%%%%%%%%%%%%%%%%%%%%%%%%%%%%%%%%%%%%%%
%%%%%%%%%%%%%%%%%%%%%%%%%%%%%%%%%%%%%%%%%%%%%%%%%%%%%%%%%%
Hw=1.10e-9; %QD height
ita=3.5755; %effective refractive index
Nl=5; %number of QD layers
ND=3e14;%QD surface density change from 3e14 to 2e14
N=15; %number of QD groups
D_ES=4; %degeneracy of ES
D_GS=2; %degeneracy of GS

tau_cW=1.2e-12; %capture time to WL
tau_cES=1.2e-12; %capture time to ES
tau_cGS=1.2e-12; %capture time to GS
tau_rW=100e-12; %interband recombination time in WL
tau_sES=500e-12; %spontaneous emission time of ES1
tau_sGS=1200e-12; %spontaneous emission time of GS

beta_sp=1e-4; %spontaneous emission factor
alpha=1700; %internal modal loss
Gammaxy=0.07; %optical confinement factor

steps=15;

%%Device Parameters%%%%%%%%%%%%%%%%%%%%%%%%%%%%%%%%%%%%%%%%%%%%%%%%%%%%%%%%%%
%%%%%%%%%%%%%%%%%%%%%%%%%%%%%%%%%%%%%%%%%%%%%%%%%%%%%%%%%%
W=6e-6; %ridge width
hSCH=355e-9; %height of separate confinement heterostructure
(SCH)
```

```

hW=355e-9; %width of wetting layer (WL)
r0=sqrt(0.99); %facet refractivity
rL=sqrt(0.33);
L=1.33e-3; %cavity length
l=L; %length of amplifier

I=20e-3; %current
J=I/W/L; %current density

%%Mesh%%%%%%%%%%%%%%%%%%%%%%%%%%%%%%%%%%%%%%%%%%%%%%%%%%%%%%%%%%
%%%%%%%%%%%%%%%%%%%%%%%%%%%%%%%%%%%%%%%%%%%%%%%%%%%%%%%%%%
Vg=c/ita; %speed of light (cavity)
dt=20e-15; %time spacing
dz=dt*Vg; %distance spacing
NNz=round(L/dz); %number of distance steps
tend=80e-12; %end time

%%%%%%%%%%%%%%%%%%%%%%%%%%%%%%%%%%%%%%%%%%%%%%%%%%%%%%%%%%
%%%%%%%%%%%%%%%%%%%%%%%%%%%%%%%%%%%%%%%%%%%%%%%%%%%%%%%%%%
m_effSCH=0.073*m0; %effective carrier mass in SCH
m_effQW=0.064*m0; %effective carrier mass in QW
m_effQD=0.027*m0; %effective carrier mass in QD

T=300; %temperature

df=c/2/ita/L; %frequency spacing
dE=h*df; %energy spacing
Lw_h=0.008*e; %homogeneous gain broadening
Lw_ES=0.045*e; %inhomogeneous gain broadening in ES
Lw_GS=0.0366*e; %inhomogeneous gain broadening in GS
d_ES=0.96e-9*e; %dipole matrix element of ES
d_GS=0.6e-9*e; %dipole matrix element of GS
A_ES=d_ES^2*pi/epsilon0;
A_GS=d_GS^2*pi/epsilon0;
Gamma=Lw_h/hbar; %dephasing rate of interband transition

energy_ES=0.856*e; %recombination energy of ES
energy_GS=0.806*e; %recombination energy of GS

%%Preallocation%%%%%%%%%%%%%%%%%%%%%%%%%%%%%%%%%%%%%%%%%%%%%%%%%%%%%%%%%%
%%%%%%%%%%%%%%%%%%%%%%%%%%%%%%%%%%%%%%%%%%%%%%%%%%%%%%%%%%
Ef=zeros(NNz+1,length(time));Eb=zeros(NNz+1,length(time));
%electric field (+ and -)
Eftemp=zeros(NNz+1,1);Ebtemp=zeros(NNz+1,1); %temporary electric
field (+ and -)

```

```

prob_ES=zeros(NNz+1,length(time),N);prob_GS=zeros(NNz+1,length(ti
me),N); %occupation probability
If_ES=zeros(NNz+1,length(time),N);Ib_ES=zeros(NNz+1,length(time),
N); %convolution in polarization expression for ES
If_GS=zeros(NNz+1,length(time),N);Ib_GS=zeros(NNz+1,length(time),
N); %convolution in polarization expression for GS
If_sp_ES=zeros(NNz+1,length(time),N);Ib_sp_ES=zeros(NNz+1,length(
time),N); %convolution in polarization expression of spontaneous
emission for ES
If_sp_GS=zeros(NNz+1,length(time),N);Ib_sp_GS=zeros(NNz+1,length(
time),N); %convolution in polarization expression of spontaneous
emission for GS
pf_ES=zeros(NNz+1,length(time),N);pb_ES=zeros(NNz+1,length(time),
N); %polarization expression for ES
pf_GS=zeros(NNz+1,length(time),N);pb_GS=zeros(NNz+1,length(time),
N); %polarization expression for GS
N_SCH=zeros(NNz+1,length(time));N_W=zeros(NNz+1,length(time));
%carrier density on SCH and WL
N_stimES=zeros(NNz+1,1); %stimulated emission absorption in ES
N_stimGS=zeros(NNz+1,1); %stimulated emission absorption in GS
tau_eES=zeros(1,N);tau_eGS=zeros(1,N); %electron lifetime
tau_sp_ES=zeros(1,N);tau_sp_GS=zeros(1,N); %spontaneous emission
lifetime
Omega_ES=zeros(1,N);Omega_GS=zeros(1,N); %emission frequency
Chi=zeros(20000,length(time));Chin=zeros(20000,length(time));
gain=zeros(20000,length(time));
G1=zeros(1,N); %dot size distribution
phif_ES=2*pi*rand(NNz+1,length(time),N);phib_ES=2*pi*rand(NNz+1,l
ength(time),N); %uniformly distributed between 0 and 2*pi and
uncorrelated in time
phif_GS=2*pi*rand(NNz+1,length(time),N);phib_GS=2*pi*rand(NNz+1,l
ength(time),N);

Pf1=zeros(NNz+1,length(time));Pb1=zeros(NNz+1,length(time));
%total polarization (+ and -)
Pf2=zeros(NNz+1,length(time));Pb2=zeros(NNz+1,length(time));
%%%%%%%%%%%%%%%%%%%%%%%%%%%%%%%%%%%%%%%%%%%%%%%%%%%%%%%%%%%%%%%%%%%%%%%%
%%%%%%%%%%%%%%%%%%%%%%%%%%%%%%%%%%%%%%%%%%%%%%%%%%%%%%%%%%%%%%%%%%%%%%%%

for nn=1:N
    Omega_ES(nn)=(energy_ES+(nn-(N+1)/2)*N*dE)/hbar;
    Omega_GS(nn)=(energy_GS+(nn-(N+1)/2)*N*dE)/hbar;
end

deltaE_SCHQW=0.050*e; %SCH-WL energy separation

```

```

EOmega_W=0.040*e+Omega_ES((N+1)/2)*hbar; %WL-ES energy separation
40meV
%omega0=Omega_GS((N+1)/2); %central frequency
DOS_SCH=2*(2*pi*m_effSCH*kB*T/h^2)^1.5; %DOS in SCH
DOS_W=m_effQW*kB*T/pi/hbar^2; %DOS in WL

%%%%%%%%%%%%%%%%%%%%%%%%%%%%%%%%%%%%%%%%%%%%%%%%%%%%%%%%%%%%%%%%%%%%%%%%%
%%%%%%%%%%%%%%%%%%%%%%%%%%%%%%%%%%%%%%%%%%%%%%%%%%%%%%%%%%%%%%%%%%%%%%%%%
G1(1:N)=exp(-4*log(2)*(hbar*(Omega_GS(1:N)-Omega_GS((N+1)/
2))).^2/Lw_GS^2);
Z=sum(G1); %normalization constant
Gx=G1/Z; %normalized dot size distribution

%%%%%%%%%%%%%%%%%%%%%%%%%%%%%%%%%%%%%%%%%%%%%%%%%%%%%%%%%%%%%%%%%%%%%%%%%
%%%%%%%%%%%%%%%%%%%%%%%%%%%%%%%%%%%%%%%%%%%%%%%%%%%%%%%%%%%%%%%%%%%%%%%%%
tau_eES(1:N)=tau_cES*D_ES*ND/DOS_W*exp((EOmega_W-
hbar*Omega_ES(1:N))/kB/T); %escape time from GS
tau_eGS(1:N)=tau_cGS*D_GS/D_ES*exp((hbar*Omega_ES(1:N)-
hbar*Omega_GS(1:N))/kB/T); %escape time from ES
tau_eW=tau_cW*DOS_W*Nl/DOS_SCH/hSCH*exp(deltaE_SCHQW/kB/T);
%escape time from WL
tau_sp_ES(1:N)=1./(A_ES*ita*Omega_ES(1:N).^3/(pi^2*c^3*hbar));
%spontaneous emission time for ES
tau_sp_GS(1:N)=1./(A_GS*ita*Omega_GS(1:N).^3/(pi^2*c^3*hbar));
%spontaneous emission time for GS

Times=0;
s0=0.25; %unsaturated loss
Ssat=0.04; %saturation intensity
delta=14.801; %Kerr-coefficient
dng=-5.1e5; %dng/dlambda
lambda0=1.225e-6;
omega0=c/(lambda0/2/pi);
beta2=-1*lambda0^2/2/pi/c^2*dng; %dispersion coefficient

spdzf=zeros(NNz+1); spdzb=zeros(NNz+1);

for n=1:N
    for t=1:length(time)
        prob_ES(1:NNz+1,t,n)=N_ES(t)/Nl/ND/Gx(n)/D_ES/W/dz;
%occupation probability
        prob_GS(1:NNz+1,t,n)=N_GS(t)/Nl/ND/Gx(n)/D_GS/W/dz;
    end
end

```

```

    for t=2:length(time)
        If_ES(1:NNz+1,t,n)=exp(1i*(Omega_ES(n)-omega0)*dt-
Gamma*dt)*If_ES(1:NNz+1,t-1,n)+...
            1/2*dt*(Ef(1:NNz+1,t)+exp(1i*(Omega_ES(n)-omega0)*dt-
Gamma*dt)*Ef(1:NNz+1,t-1));
        Ib_ES(1:NNz+1,t,n)=exp(1i*(Omega_ES(n)-omega0)*dt-
Gamma*dt)*Ib_ES(1:NNz+1,t-1,n)+...
            1/2*dt*(Eb(1:NNz+1,t)+exp(1i*(Omega_ES(n)-omega0)*dt-
Gamma*dt)*Eb(1:NNz+1,t-1)); %convolution terms
        If_GS(1:NNz+1,t,n)=exp(1i*(Omega_GS(n)-omega0)*dt-
Gamma*dt)*If_GS(1:NNz+1,t-1,n)+...
            1/2*dt*(Ef(1:NNz+1,t)+exp(1i*(Omega_GS(n)-omega0)*dt-
Gamma*dt)*Ef(1:NNz+1,t-1));
        Ib_GS(1:NNz+1,t,n)=exp(1i*(Omega_GS(n)-omega0)*dt-
Gamma*dt)*Ib_GS(1:NNz+1,t-1,n)+...
            1/2*dt*(Eb(1:NNz+1,t)+exp(1i*(Omega_GS(n)-omega0)*dt-
Gamma*dt)*Eb(1:NNz+1,t-1));
    end

    pf_ES(1:NNz+1,:,n)=(1i/hbar*omega0/2/pi/c/ita*Gammaxy/Hw*ND*Gx(n)
*D_ES*A_ES*(2*prob_ES(1:NNz+1,:,n)-1)).*If_ES(1:NNz+1,:,n);
    %polarization contributions

    pb_ES(1:NNz+1,:,n)=(1i/hbar*omega0/2/pi/c/ita*Gammaxy/Hw*ND*Gx(n)
*D_ES*A_ES*(2*prob_ES(1:NNz+1,:,n)-1)).*Ib_ES(1:NNz+1,:,n);

    pf_GS(1:NNz+1,:,n)=(1i/hbar*omega0/2/pi/c/ita*Gammaxy/Hw*ND*Gx(n)
*D_GS*A_GS*(2*prob_GS(1:NNz+1,:,n)-1)).*If_GS(1:NNz+1,:,n);

    pb_GS(1:NNz+1,:,n)=(1i/hbar*omega0/2/pi/c/ita*Gammaxy/Hw*ND*Gx(n)
*D_GS*A_GS*(2*prob_GS(1:NNz+1,:,n)-1)).*Ib_GS(1:NNz+1,:,n);

    Pf1(1:NNz+1,:)=Pf1(1:NNz+1,:)+pf_ES(1:NNz+1,:,n); %sum up
    polarization terms
    Pb1(1:NNz+1,:)=Pb1(1:NNz+1,:)+pb_ES(1:NNz+1,:,n);
    Pf2(1:NNz+1,:)=Pf2(1:NNz+1,:)+pf_GS(1:NNz+1,:,n);
    Pb2(1:NNz+1,:)=Pb2(1:NNz+1,:)+pb_GS(1:NNz+1,:,n);

    If_sp_ES(1:NNz+1,2:length(time),n)=exp(1i*(Omega_ES(n)-
omega0)*dt-Gamma*dt)*If_sp_ES(1:NNz+1,1:length(time)-1,n)+...
        1/2*dt*(exp(1i*phif_ES(1:NNz+1,2:length(time),n))
+exp(1i*(Omega_ES(n)-omega0)*dt-

```



```

Gamma*dt+1i*phif_ES(1:NNz+1,1:length(time)-1,n)); %convolution
terms for spontaneous emission
    Ib_sp_ES(1:NNz+1,2:length(time),n)=exp(1i*(Omega_ES(n)-
omega0)*dt-Gamma*dt)*Ib_sp_ES(1:NNz+1,1:length(time)-1,n)+...
    1/2*dt*(exp(1i*phib_ES(1:NNz+1,2:length(time),n))
+exp(1i*(Omega_ES(n)-omega0)*dt-
Gamma*dt+1i*phib_ES(1:NNz+1,1:length(time)-1,n)));
    If_sp_GS(1:NNz+1,2:length(time),n)=exp(1i*(Omega_GS(n)-
omega0)*dt-Gamma*dt)*If_sp_GS(1:NNz+1,1:length(time)-1,n)+...
    1/2*dt*(exp(1i*phif_GS(1:NNz+1,2:length(time),n))
+exp(1i*(Omega_GS(n)-omega0)*dt-
Gamma*dt+1i*phif_GS(1:NNz+1,1:length(time)-1,n)));
    Ib_sp_GS(1:NNz+1,2:length(time),n)=exp(1i*(Omega_GS(n)-
omega0)*dt-Gamma*dt)*Ib_sp_GS(1:NNz+1,1:length(time)-1,n)+...
    1/2*dt*(exp(1i*phib_GS(1:NNz+1,2:length(time),n))
+exp(1i*(Omega_GS(n)-omega0)*dt-
Gamma*dt+1i*phib_GS(1:NNz+1,1:length(time)-1,n)));

    for z=1:NNz+1

spdzf(z)=sum(Gamma*(sqrt(hbar*Omega_ES(n)/(pi*Gamma*dt))*(beta_sp*
N_ES(t))/(2*tau_sp_ES(n))).*If_sp_ES(z,:,n))+... %spontaneous
emission noise

sqrt(hbar*Omega_GS(n)/(pi*Gamma*dt))*(beta_sp*N_GS(t)/(2*tau_sp_GS
(n))))).*If_sp_GS(z,:,n));

spdzb(z)=sum(Gamma*(sqrt(hbar*Omega_ES(n)/(pi*Gamma*dt))*(beta_sp*
N_ES(t))/(2*tau_sp_ES(n))).*Ib_sp_ES(z,:,n))+...

sqrt(hbar*Omega_GS(n)/(pi*Gamma*dt))*(beta_sp*N_GS(t)/(2*tau_sp_GS
(n))))).*Ib_sp_GS(z,:,n));
    end
end

for z=1:NNz+1 %NaN check
    for t=1:length(time)-1
        if z~=NNz+1; Ef(z+1,t+1)=(Ef(z,t)-1i*(Pf1(z,t)
+Pf2(z,t))*dz+spdzf(z)-alpha/2*Ef(z,t)*dz)*exp(-
1i*delta*abs(Ef(z,t))^2*dz); end
        if z~=1; Eb(z-1,t+1)=(Eb(z,t)-1i*(Pb1(z,t)
+Pb2(z,t))*dz+spdzb(z)-alpha/2*Eb(z,t)*dz)*exp(-
1i*delta*abs(Eb(z,t))^2*dz); end
        if isnan(abs(Ef(z,t))^2)
            keyboard; end
    end
end

```

```

        end
    end

    for t=1:length(time)-1

        Ef(NNz+1,t+1)=(1-s0/(1+(abs(Ef(NNz,t))^2/Ssat)^1))*Ef(NNz+1,t+1);
        %self-focusing
        Eb(NNz+1,t+1)=rL*Ef(NNz+1,t+1); %boundary conditions
        Ef(1,t+1)=r0*Eb(1,t+1);
    end

    %%%%%%%%%%%%%%%%%%%%%%%%%%%%%%%%%%%%%%%%%%%%%%%%%%%%%%%%%%%%%%%%%%%%%%%%%
    %%%%%%%%%%%%%%%%%%%%%%%%%%%%%%%%%%%%%%%%%%%%%%%%%%%%%%%%%%%%%%%%%%%%%%%%%
    Eout=sqrt(1-rL^2)*Ef(NNz+1,:); %output
    save('Eoutput','Eout');

    Ef(1:NNz+1,1:2)=Ef(1:NNz+1,length(time)-
    1:length(time));Eb(1:NNz+1,1:2)=Eb(1:NNz+1,length(time)-
    1:length(time));
    N_SCH(1:NNz+1,1:2)=N_SCH(1:NNz+1,length(time)-
    1:length(time));N_W(1:NNz+1,1:2)=N_W(1:NNz+1,length(time)-
    1:length(time));

    t1=round(length(Eout)/10);
    t2=length(Eout);
    dt=time(3)-time(2);
    E=Eout(t1:t2);
    df=1/(t2-t1+1)/dt;
    fmax=1/dt/2;
    fFFT=round(-fmax:df:fmax-df);
    f0=omega0/2/pi;
    lambdaFFT=c./(fFFT+f0);
    x=t2-t1;
    F=(abs(fftshift(fft(E))))).^2/x^2;
    F_dBm=10*log10(F/mean(F));
    Fmax_dBm=max(F_dBm);
    norm_spectrum=F_dBm-Fmax_dBm;
    compat=pwelch('psd');
    [pxx,f]=pwelch(E/mean(E),length(fFFT));
    pwelch(compat);
    f_m=linspace(f(1),f(length(f)),length(F_dBm));
    P=E.*conj(E)/1e-3;
    Pavg=mean(P);

```

```

omega=linspace(2*pi*220e12,2*pi*280e12,20000);
lambda=c./(omega/2/pi);

figure(1);
plot(time/1e-12,Eout.*conj(Eout)/1e-3);xlim([0,time(t2)/1e-12]);
ylim([min(Eout.*conj(Eout)/1e-3),max(Eout.*conj(Eout)/1e-3)]);
xlabel('Time (ps)');ylabel('Intensity (mW)');

figure(2);
plot(time(t1:t2)/1e-12,P);xlim([time(t1)/1e-12,time(t2)/1e-12]);
ylim([min(P),max(P)]);xlabel('Time (ps)');ylabel('Intensity
(mW)');

figure(3);
plot(lambdaFFT/1e-9,F_dBm);grid;xlabel('Wavelength [nm]');
xlim([(lambda0/1e-9)-30,(lambda0/1e-9)+30]);ylabel('Optical
Spectrum [dBm]');

figure(4);
plot(lambdaFFT/1e-9,F_dBm);grid;xlabel('Wavelength [nm]');
xlim([(lambda0/1e-9)-20,(lambda0/1e-9)+20]);ylabel('Optical
Spectrum [dBm]');

figure(5);
plot(lambdaFFT/1e-9,F_dBm);grid;xlabel('Wavelength [nm]');
xlim([(lambda0/1e-9)-10,(lambda0/1e-9)+10]);ylabel('Optical
Spectrum [dBm]');

figure(6);
plot(lambdaFFT/1e-9,norm_spectrum);grid;xlabel('Wavelength
[nm]');
ylabel('Normalized Opt. Spec. [dB]');

figure(7);
plot(f,10*log10(pxx));grid;xlabel('Frequency [Hz]');ylabel('Opt.
Spec. [dB]');

figure(8);
plot(f_m,F_dBm);grid;xlabel('Frequency [Hz]');ylabel('Opt. Spec.
[dB]');

figure(9);
plot(c./(lambdaFFT/1e-9),norm_spectrum);grid;xlabel('Frequency
[Hz]');
ylabel('Opt. Spec. [dB]');

```